



# **Analysis of wrinkled membrane structures using a Plane Stress projection procedure and the Dynamic Relaxation method**

H. Le Meitour, G. Rio, H. Laurent, A.S. Lectez, P. Guigue

## **► To cite this version:**

H. Le Meitour, G. Rio, H. Laurent, A.S. Lectez, P. Guigue. Analysis of wrinkled membrane structures using a Plane Stress projection procedure and the Dynamic Relaxation method. *International Journal of Solids and Structures*, 2021, 208-209, pp.194-213. <10.1016/j.ijssolstr.2020.10.026>. <hal-04649889>

**HAL Id: hal-04649889**

**<https://hal.science/hal-04649889v1>**

Submitted on 18 Nov 2024

**HAL** is a multi-disciplinary open access archive for the deposit and dissemination of scientific research documents, whether they are published or not. The documents may come from teaching and research institutions in France or abroad, or from public or private research centers.

L'archive ouverte pluridisciplinaire **HAL**, est destinée au dépôt et à la diffusion de documents scientifiques de niveau recherche, publiés ou non, émanant des établissements d'enseignement et de recherche français ou étrangers, des laboratoires publics ou privés.



HAL Authorization

# Analysis of wrinkled membrane structures using a Plane Stress projection procedure and the Dynamic Relaxation method

H. Le Meitour<sup>a</sup>, G. Rio<sup>a</sup>, H. Laurent<sup>a,\*</sup>, A. S. Lectez<sup>b</sup>, P. Guigue<sup>b</sup>

<sup>a</sup> *Univ. Bretagne Sud,*

*UMR CNRS 6027, IRDL, F-56100 Lorient, France*

<sup>b</sup> *CNES, Centre Spatial de Toulouse,*

*18 avenue Edouard Belin, F-31401 Toulouse cedex 9, France*

---

## Abstract

Deployable membrane structures such as inflatable stratospheric balloons are known to be sensitive to the occurrence of local instabilities such as wrinkles. The wrinkling phenomenon affects the working performances of the membrane and the occurrence of this phenomenon has to be controlled numerically in order to predict the best means of deployment during the inflation of aerospace balloons. To improve their performances and reliability during flight, the balloons also need to be sized appropriately without the stress field being disturbed by the wrinkles. These instabilities originate numerically from the membrane elements which have a negligible bending stiffness. Several wrinkling models have been presented in the literature in order to solve this problem. However, in most of these models an elastic law and the Green deformation approach have been used for this purpose.

The new model called the PS-DPS model presented here for correcting the effects of wrinkles on membrane structures was implemented in the in-

---

\*Corresponding author

*Email address:* `herve.laurent@univ-ubs.fr` (H. Laurent)

*URL:* `http://irdl.fr/` (H. Laurent)

house finite element software Herezh++. A projection technique based on a Newton-Raphson method is used to control the stress plane and the in-plane contraction. Using the Almansi strain formulation, this model also accounts for the changes in membrane thickness liable to occur during simulations. The problems due to numerical instabilities are overcome by determining the equilibrium with the so-called Dynamic Relaxation method using kinetic damping procedures. Unlike other membrane models of literature, the PS-DPS model can be used with materials showing complex mechanical behaviour of all kinds. Several benchmark problems are analysed with the present wrinkling model and compared with results available in the literature, focusing first on an elastic law and then on a non-linear hyperelastic law. Lastly, the inflation of a square cushion test and that of a Zero Pressure Balloon are simulated with this non-linear law. The results obtained indicate that the PS-DPS model is valid and accurate to take into account the wrinkles in flexible structures with all these linear and non-linear behaviours.

*Keywords:* Wrinkling model, Membrane structures, Inflated structures, Dynamic Relaxation method, Plane Stress projection procedure, Non-linear behaviour

---

## 1. Introduction

Inflated stratospheric balloons made of thin plastic film are widely used by the French Space Agency (CNES) for studying atmospheric and astrophysical phenomena and testing technological innovations. Due to the large size of these balloons (which measure anything up to 180 m in height) and the flexibility of their polyethylene envelope (which is only a few tens of  $\mu\text{m}$  thick), inflation of the stratospheric balloons causes local buckling phenomena, which appears as wrinkling. These buckling processes are due to the fact that these membrane structures, which have been referred to as "without compression", have a negligible bending stiffness. If no compressive stress is induced in the membrane, an out-of-plane displacement of the membrane will occur, resulting in wrinkles.

The number of numerical studies on wrinkled structures such as flexible membranes and fine fabric structures has increased considerably since the 1990s. Jenkins in his 1996 review [\[1\]](#) was the first to not only outline the problem of wrinkling, but also to cover all the aspects of the theory and applications of thin structures that can be defined as membranes. Several reviews [\[2–9\]](#) have been subsequently published on the various finite element methods developed for simulating wrinkling problems. The basic idea was introduced by Wagner [\[10\]](#), based in particular on Tension-Field (TF) theory, and on the assumption that a membrane has no bending stiffness and cannot resist any compression forces. Many wrinkling models (see for example [\[6; 11\]](#)) have since been developed on these lines for predicting the wrinkling direction and eliminating the in-plane stiffness in the direction perpendicular to the wrinkles.

Thus, the first type of wrinkling model was to modify the deformation gradient tensor to represent TF responses of wrinkled membranes [\[12; 13\]](#).

28 By introducing the concept of relaxed energy density, Pipkin <14> defined  
29 membrane wrinkling as a problem of energy minimization arising in the case  
30 of elastic bodies devoid of bending rigidity. This method inspired several  
31 other models <15–17>, and Epstein and Forcinito <18> extended this re-  
32 laxated energy function model to include anisotropic membranes by introducing  
33 the idea of saturated elasticity and by modifying the Green’s strain tensor.

34 The second approach, on which this paper focuses, is based on a local  
35 modification of the stress-strain relationship within an element, *i.e.* the  
36 constitutive equation is modified in order to eliminate all the compressive  
37 stresses <19>. In this case, there exist several possible solutions. One of  
38 them consists in modifying the stiffness tensor of elasticity by adding a cor-  
39 rective factor <4; 20–22>. Another one consists in modifying the constants  
40 of the material such as the modulus of elasticity and/or the Poisson’s ratio  
41 <23–26>. Another method consists in post-multiplying the stiffness matrix  
42 with a projection matrix that eliminates the compressive stresses <19; 27>.  
43 The influence of these various solutions can be seen in the paper by Wang  
44 et al. <6>. These previous approaches provide a rigorous mathematical  
45 formulation of the wrinkling mechanism and can easily be applied to existing  
46 finite element codes for the analysis of membrane structures with wrinkles.  
47 However, the exact physical significance of the modified elasticity matrix is  
48 somewhat obscure because of the arbitrary choice of projection matrix.

49 The last approach to modelling wrinkles worth mentioning consists in  
50 using thin shell elements that include both membrane and bending contribu-  
51 tions and can be used to model the amplitude and wavelength of wrinkles.  
52 This method has been adopted in several studies (*e.g.* <3; 28>). Unfor-  
53 tunately, in order to obtain sufficiently realistic results, the mesh size must  
54 be sufficiently fine which requires fairly long computational times. Shell el-

55 elements are naturally more expensive in terms of computational time than  
 56 membrane elements because a large number of degrees of freedom (rota-  
 57 tions) and integration points (through the thickness) is required. During the  
 58 last few years, however, shell elements devoid rotational degrees of freedom  
 59 have been developed <29–32> and used to model the shape of wrinkles on  
 60 isotropic and anisotropic flexible structures <33>. Elements of this kind are  
 61 the most efficient for modelling the wrinkles phenomena in small structures,  
 62 but in the case of large structures such as stratospheric balloons, this option  
 63 does not seem to be the most efficient due to the long computational times  
 64 induced by the mesh size. In addition, it is worth noting that the wrinkling  
 65 behaviour (*i.e.* buckling) often depends on the size and type of mesh.

66 Finding suitable means of modelling wrinkling processes in the design  
 67 stage is therefore an important challenge for constructing reliable membrane-  
 68 based space structures <34>. It is of the utmost importance to be able to  
 69 predict the behaviour of membrane wrinkles, including the direction in which  
 70 they occur and what stresses are at work in the case of inflated stratospheric  
 71 balloons <11>. However, most previous studies have focused so far on de-  
 72 termining the direction of the wrinkling process and the corresponding stress  
 73 state in the case of materials with isotropic <7; 14; 35> or anisotropic linear  
 74 behaviour <12; 17; 18; 22; 36> as well as for linear viscoelastic behaviour  
 75 <37–40>. However, in the case of materials with non linear behaviour, this  
 76 subject still requires further investigation <41; 42>, and in the context of  
 77 stratospheric balloons, it should be noted that thin films show complex be-  
 78 haviour characterized by large irreversible strains and strain rate dependency,  
 79 and therefore, elasto-visco-plastic behaviour. In this context, the aim of this  
 80 paper is to present a new simple, accurate method of modelling membrane  
 81 structures giving the wrinkling directions for all kinds of material behaviours.

82 This model, which we have called the "Plane Stress-Double Plane Stress"  
83 (PS-DPS) model, is based on two approaches. The first approach consists in  
84 adjusting the components of the constitutive tensor in the direction of the  
85 compressive stress. The principle underlying this method is in fact consistent  
86 with other approaches used in <4; 19; 43>, for example, but the Newton-  
87 Raphson method of projection used here makes it possible to control the  
88 constitutive matrix in the case of materials of all kinds. In this case, the aim  
89 is not to simulate the shape of the wrinkles but to account for their occurrence  
90 on the equilibrium state of the membrane. Another originality feature of this  
91 model is that the thickness of the membrane structure is updated throughout  
92 the simulation.

93 The second approach used in the PS-DPS model overcomes the numeri-  
94 cal instabilities that are liable to occur due to the poor convergence of the  
95 numerical resolution of the membrane structure. This is can be explained  
96 by the fact that the local stiffness of the membrane can vary between large  
97 positive values and zero during the iterative process. A Dynamic Relaxation  
98 (DR) method (which is also known as the pseudo-Dynamic method) is then  
99 introduced to determine the global equilibrium in the analysis of undercon-  
100 strained membranes <44; 45>.

101 These two approaches and the DR method are implemented in the in-  
102 house finite element software Herezh++ <46-48>. In the literature, wrinkled  
103 membrane models have been classically written based on the initial config-  
104 uration of the structure using the Green strain tensor <6; 7; 27> whereas  
105 the PS-DPS model is written here based on the current configuration of the  
106 structure using the Almansi strain measure and the Cauchy stress tensor.

107 This paper is structured as follows: the numerical methods used to de-  
108 velop the PS-DPS model are presented in Section 2. The distinctive char-

109 acteristics of the Plane Stress and Double Plane Stress approaches are ex-  
 110 plained in sections 2.3 and 2.4 respectively. The pseudo-Dynamic process  
 111 is then described in section 3. To show the accuracy and potential of the  
 112 present model, several benchmark examples are modelled and analysed in  
 113 section 4 using isotropic elastic law and compare with results available in the  
 114 literature. First, structures constrained in their planes are studied. Shear  
 115 test is first analysed since this is the most widely used test for checking the  
 116 validity of wrinkling models. In this test, the membrane is fully wrinkled  
 117 (in either a single direction or all possible directions) in order to check the  
 118 accuracy of the PS-DPS model. The results of a torsion test in which the  
 119 membrane shifts locally from a wrinkled to a taut state is then compared  
 120 with an analytical solution. Next, a square cushion deployment is carried  
 121 out in order to test the model on a structure resembling that of stratospheric  
 122 balloon. In this test, comparisons are also made with finite element simula-  
 123 tions performed with Abaqus <49> using the "No compression" procedure,  
 124 in which the elastic behaviour is modified by imposing the appropriate prin-  
 125 cipal stress at zero. To determine the influence of behavioral laws on the  
 126 results obtained, the inflation of a square cushion test is also simulated using  
 127 a hyperelastic law with the PS-DPS model in section 4.4. Lastly, in section 5,  
 128 to show the applicability of the PS-DPS model in a real case of balloon in-  
 129 flation, simulations of the deployment of a Zero Pressure Balloon with both  
 130 elastic and non linear laws are presented.

## 131 2. The PS–DPS model

132 Before presenting the PS–DPS model, some notations are introduced in  
 133 order to explain the kinematic hypotheses and tensor notations used. First,  
 134 let us take a Gauss point  $M$  and the associated material frame  $\{M, \vec{g}_i\}$  (where



135  $i = 1 \dots 3$ ). The covariant base vectors, which follow the point  $M$  as a func-  
 136 tion of time  $t$ , are defined in the tangent membrane plane, using a curvilinear  
 137 coordinate system  $\theta^\alpha$ , by:

$$\vec{g}_\alpha(t) = \frac{\partial \vec{M}_{(t)}}{\partial \theta^\alpha} \text{ with } \alpha = 1, 2 \quad (1)$$

138 In the Herezh++ software, these curvilinear coordinates constituting a set  
 139 of material coordinates are those used in the base of the reference element  
 140 (for further details, see for instance <30; 50>). The normal vector of the  
 141 tangent plane is obtained by taking  $\vec{g}_3 = \vec{g}_1 \wedge \vec{g}_2$ . The norm of  $\vec{g}_3$  is arbitrarily  
 142 set at 1 (see fig. 1).

143 The contravariant components  $\sigma^{ij}$  of the Cauchy stress tensor  $\boldsymbol{\sigma}$  are de-  
 144 fined at each Gauss Point  $M$  in the current configuration using these covari-  
 145 ant base vectors according to:

$$\boldsymbol{\sigma} = \sigma^{ij} \vec{g}_i \otimes \vec{g}_j \quad (2)$$

146 The Almansi strain tensor can also be defined in the contravariant current  
 147 base vector taking:

$$\boldsymbol{\epsilon} = \epsilon_{ij} \vec{g}^i \otimes \vec{g}^j \quad (3)$$

## 148 2.1. Evaluation of the membrane states

149 In the literature, to denote the various states of the membrane (taut,  
 150 slacked and wrinkled), three criteria based on the signs of the components  
 151  $\sigma_I$  and  $\sigma_{II}$  of the principal stresses and/or the principal strains  $\epsilon_I$  and  $\epsilon_{II}$  are  
 152 now widely used (see table 1).

153 According to Liu et al. <21>, the stress criterion underestimates the state  
 154 of "slackness" and the strain criterion underestimates the state of "tautness"  
 155 of the membrane. Several authors <20; 51> have suggested that the mixed  
 156 criterion seems to be the most useful means of differentiating between these

Membrane states	Stress criterion	Strain criterion	Mixed criterion
Taut	$\sigma_{II} > 0$	$\varepsilon_{II} > 0$	$\sigma_{II} > 0$
Wrinkled	$\sigma_{II} < 0 \ \& \ \sigma_I > 0$	$\varepsilon_{II} < 0 \ \& \ \varepsilon_I > 0$	$\sigma_{II} < 0 \ \& \ \varepsilon_I > 0$
Slacked	$\sigma_I < 0$	$\varepsilon_I < 0$	$\varepsilon_I < 0$

Table 1: The three membrane states defined by the stress, strain and mixed criteria as a function of the principal stresses and strains.

states. Wang et al. [\[6\]](#) recently presented a new means of modelling these three states, taking the previous state obtained in the membrane and a combination between the stress criterion and the strain criterion. This new approach seems to be as effective as the mixed criterion but it requires the use of the Poisson’s ratio, which restricts its use to material with linear elastic behaviour. In view of this constraint, the mixed criterion was adopted in the PS–DPS model. From a numerical point of view, a first computation without taking into account the wrinkles is carried out to determine these zones.

## 2.2. Principles underlying the PS–DPS model

As mentioned above in the Introduction, there are several ways of approaching wrinkles numerically. In the PS–DPS model, the aim is not to model the shape of the wrinkles, but to predict the consequences of the presence of wrinkles on the mechanical equilibrium of the membrane. From the practical point of view, the PS–DPS is intended to apply to a wrinkled structure, regarded as a unwrinkled planar membrane. The out-of-plane displacement caused by compressive stresses is simply approached like an in-plane contraction, as shown in fig. 1.

The PS–DPS model is based on two numerical assumptions. First, in

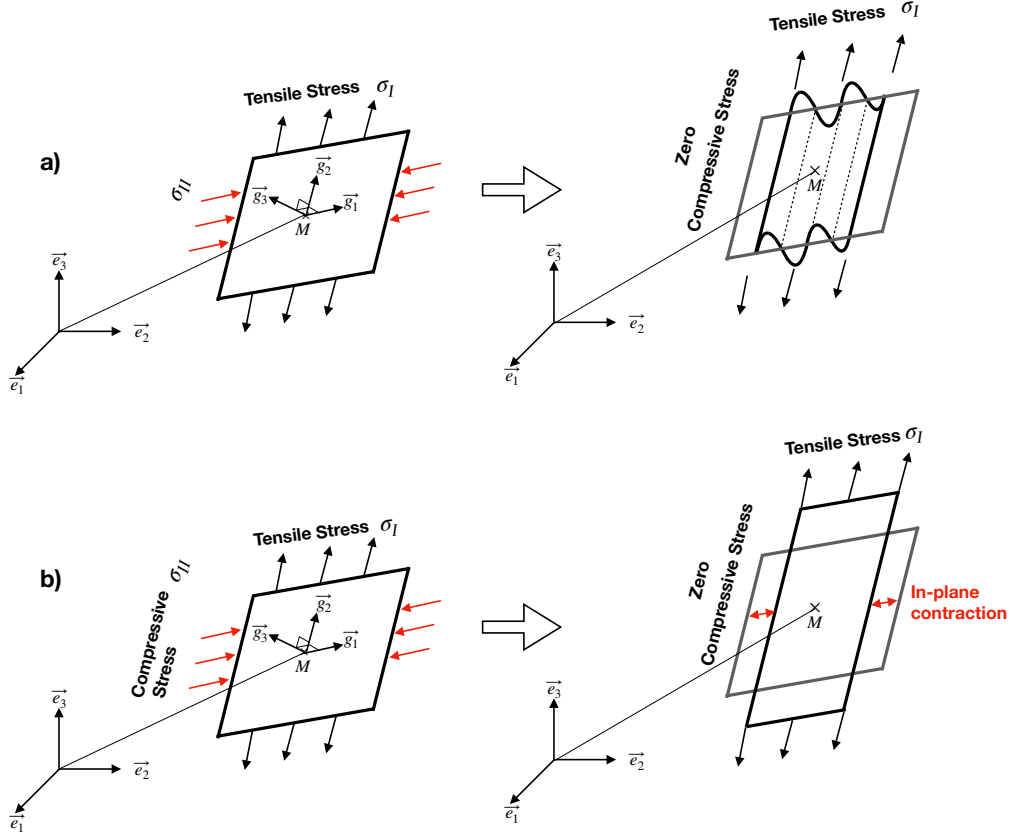


Figure 1: Diagram of the position and stress state of a Gauss point  $M$  in the membrane plane formed by  $(\vec{g}_1, \vec{g}_2)$  in the Cartesian coordinate system  $\vec{e}_i$ . a) Real membrane stress with wrinkles. b) Accounting for the behaviour of wrinkles with the PS–DPS model.

the case of any 3D behavioural law, a Newton-Raphson technique is used to impose a "Plane Stress" (PS) state on the membrane structures. In the second step, the assumptions of the TF theory, which we refer to here as the "Double Plane Stress" (DPS), are applied to the wrinkled part in a state of uniaxial tension on the plane of the membrane.

### 2.3. Membrane behaviour without any wrinkles: the PS state

During the equilibrium incremental, we assume that we have reached the end of an increment of time  $t + \Delta t$ , in which the kinematic displacements are

known, *i.e.* the 3D deformation state  $\boldsymbol{\varepsilon}_{(t+\Delta t)}$ , the increment of deformation  $\Delta_t^{t+\Delta t} \boldsymbol{\varepsilon}$  between  $t$  and  $t + \Delta t$ , the strain rate tensor  $\boldsymbol{D}_{(t+\Delta t)}$  and the 3D stress state  $\boldsymbol{\sigma}_{(t+\Delta t)}$  are all known.

The first step in this approach consists in finding a PS state such that  $\sigma^{3i} = 0$  as a function of the unknowns  $\varepsilon_{3i}$ , where  $i = 1 \dots 3$ , at each Gauss point  $M$ . In this case, as  $\vec{g}_3$  is assumed to be a principal direction (*i.e.* an eigenvector for stress and strain tensors) and  $\varepsilon_{31} = \varepsilon_{32} = 0$ , the sole condition which has to be found is:

$$\sigma^{33}(\varepsilon_{33}) = 0 \quad (4)$$

To obtain this no stress compression state  $\sigma^{33}(\varepsilon_{33}) = 0$ , which is denoted  $\boldsymbol{\sigma}_{(int)}$ , a scheme based on a three steps Newton-Raphson algorithm is used (see also the first algorithm scheme of the PS state in fig. 2):

1. The initial value of the strain tensor is such that  $\varepsilon_{\gamma\eta(t+\Delta t)}$  where  $\gamma, \eta = 1, 2$  is due to the kinematic displacement of the membrane at the point  $M$ , taking:  $\varepsilon_{31} = \varepsilon_{32} = 0$ . These values will stay constant during the Newton loops during the  $n$  iterations. The unknown  $\varepsilon_{33}$  is initialized at the beginning of the initial step  $n=1$ , by:  $\varepsilon_{33(t+\Delta t)}^{(n=1)} = \varepsilon_{33(t)}$
2. Do while  $\| \sigma_{(int)}^{33} \| < e_1$  where  $e_1$  is a given level of precision (in the loop on  $n$ ):

- (a) evaluate  $\sigma^{ij(n)}$  and  $\frac{\partial \sigma^{ij(n)}}{\partial \varepsilon_{kl}}$  from the 3D behaviour
- (b) calculate  $\delta \varepsilon_{33} = - \left[ \frac{\partial \sigma^{33(n)}}{\partial \varepsilon_{33}} \right]^{-1} \sigma^{33(n)}$ , resulting from the application of the condition eq. (4)
- (c) then  $\varepsilon_{33(n+1)} = \delta \varepsilon_{33} + \varepsilon_{33(n)}$  and increment  $n$  as:  $n = n + 1$
- (d) update the membrane thickness.

207 At the end of this first intermediate state "*int*", after convergence, the  
208 data obtained are:

- 209 • the 3D stress tensor  $\boldsymbol{\sigma}_{(int)}$  that satisfies the first PS condition,
- 210 • the new thickness deformation  $\varepsilon_{33(t+\Delta t)}$  and the associated new  
211 thickness  $h_{(t+\Delta t)}$  of the membrane.

212 3. In the case of an implicit scheme, the tangent matrix of the behavioural  
213 law is also calculated:  $\left[ \frac{\partial \sigma^{\alpha\beta}}{\partial \varepsilon_{\gamma\eta}} \right]$  where  $\alpha, \beta, \gamma, \eta = 1, 2$  which includes  
214 the PS condition. Details of the calculation of the tangent matrix in  
215 the PS condition are given in appendix [A](#).

216 Thanks to this process, the plane stress state can be applied to any type of  
217 mechanical behavior.

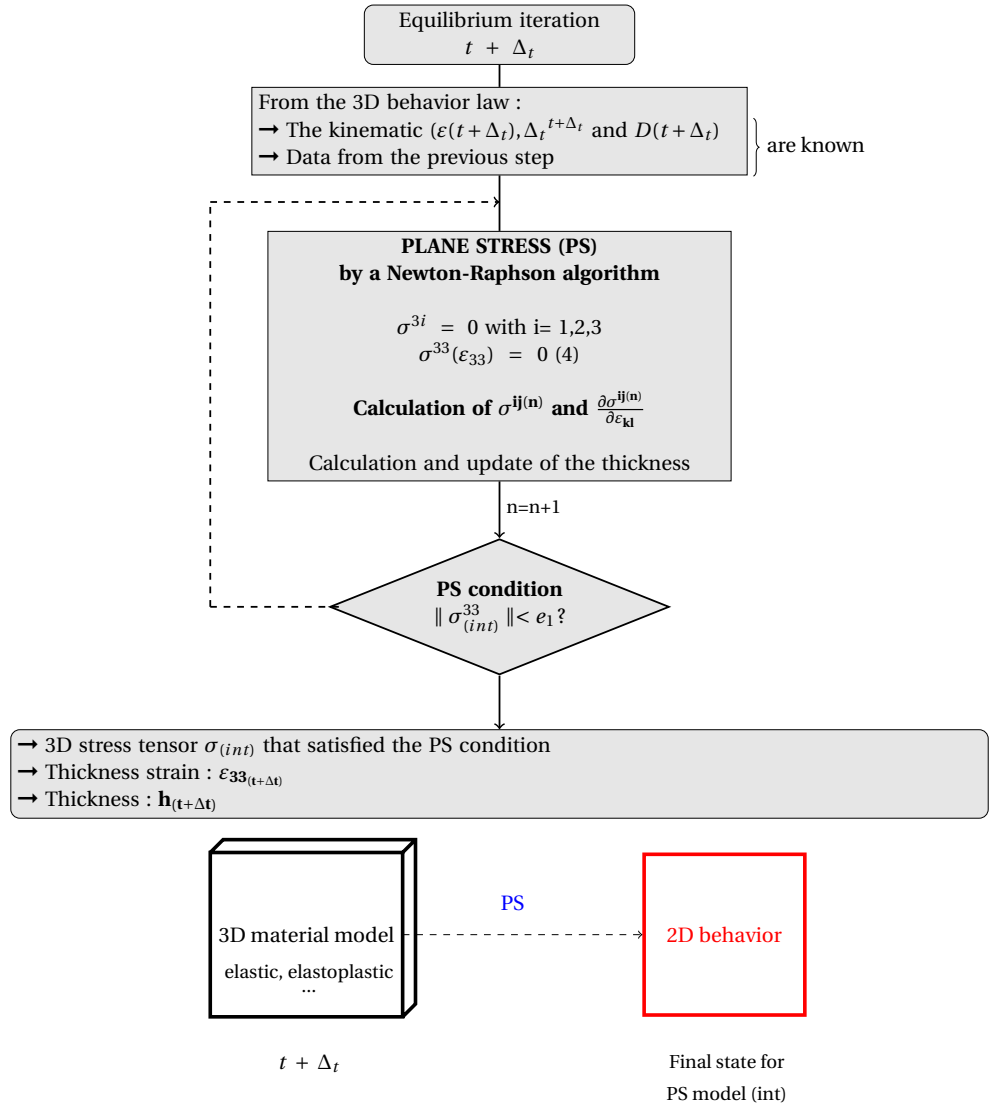


Figure 2: First algorithm used to define the PS state at a Gauss point on the membrane.

At the end of this state "*int*", the wrinkling areas are located in the membrane using the mixed criterion (see table 1). A new double plane stress (DPS) is then built into these wrinkles areas in order to release the compression by using a new Newton-Raphson algorithm (which will be discussed in the next section). The global equilibrium of the membrane is then updated with this new behaviour, which yields a new final stress  $\boldsymbol{\sigma}_{(end)}$  and strain tensors  $\boldsymbol{\varepsilon}_{(end)}$  that can be used in the next equilibrium iteration. In the tensile areas of the structure, the local state of the membrane satisfies the PS condition.

To define these wrinkled zones, eigenvalues of tensors  $\boldsymbol{\sigma}_{(int)}$  and  $\boldsymbol{\varepsilon}_{(int)}$  are calculated based on the notations  $\sigma_{(int)_I}$ ,  $\sigma_{(int)_II}$  which are the major and minor principal stresses, and  $\varepsilon_{(int)_I}$ ,  $\varepsilon_{(int)_II}$  which are the major and minor principal strains, respectively.

According to the mixed criterion (see section 2.1), the membrane could be in one of the following three states:

1.  $\sigma_{(int)_II} > 0$ : the membrane is in a state of tension in all the directions on its median plane,
2.  $\varepsilon_{(int)_I} < 0$ : the membrane lacks of tension in all the directions on its median plane,
3.  $\sigma_{(int)_II} < 0$ : there are wrinkles in the direction of the eigenvector  $\vec{V}_2$  associated with  $\sigma_{(int)_II}$ .

#### 2.4. Membrane with wrinkles: the PS–DPS Wrinkles Model

After determining the presence of wrinkles in the structure with the mixed criterion and the orientation of these wrinkles, the new stress and strain fields obtained with the DPS condition are determined using a new Newton-

243 Raphson algorithm. This DPS condition consists in imposing a new plane  
244 stress state in the direction of the wrinkles.

245 Take the eigenvector frame  $\vec{V}_\alpha$  with  $\alpha = 1, 2$ , where  $\vec{V}_1$  is the direction of  
246 the tension and  $\vec{V}_2$  the transverse direction of the wrinkles.  $\vec{V}_3$  is identical to  
247  $\vec{g}_3$  and gives a complete 3D eigenvector frame. In this frame, the presence of  
248 wrinkles must lead to  $\sigma^{22} = 0$  and the PS model implies that:  $\sigma^{33} = 0$ . So  
249 the local behaviour is like a DPS constrain and the local stress state has to  
250 be studied again with the new conditions:

$$\sigma^{\alpha\alpha} \left( \varepsilon_{11}, \varepsilon_{22(mec)} \right) = 0 \quad (5)$$

251 where  $\alpha = 2, 3$  and a new unknown  $\varepsilon_{22(mec)}$  is introduced to denote the  
252 transverse mechanical strain, which differs from the kinematic deformation  
253 of the membrane  $\varepsilon_{22(kin)}$ .

254 A Newton-Raphson scheme for the DPS state is therefore written in the  
255 frame  $\vec{V}_i$  according to the following algorithm (see also this algorithm in  
256 fig. 3):

- 257 1. Initialization of the strain tensor component:  $\varepsilon_{11(t+\Delta t)}$  with the kine-  
258 matic displacement of the membrane at the point M, taking  $\varepsilon_{12} =$   
259  $\varepsilon_{31} = \varepsilon_{32} = 0$ . These values will stay constant during the New-  
260 ton loops on the  $n$  iterations. The unknowns are initialized by:  
261  $\left\langle \varepsilon_{22(t+\Delta t)}, \varepsilon_{33(t+\Delta t)} \right\rangle^{(n=1)} = \left\langle \varepsilon_{22(t)}, \varepsilon_{33(t)} \right\rangle$  for  $n = 1$ .
- 262 2. Do while  $\| \left\langle \sigma_{(int)}^{22}, \sigma_{(int)}^{33} \right\rangle \| < e_2$  where  $e_2$  is a given precision (loop on  
263  $n$ ):

- 264 (a) evaluate  $\sigma^{ij(n)}$  and  $\frac{\partial \sigma^{ij(n)}}{\partial \varepsilon_{kl}}$  from the 3D behaviour
- 265 (b) calculate  $\langle \delta \varepsilon_{ff} \rangle = - \left[ \frac{\partial \sigma^{ee(n)}}{\partial \varepsilon_{ff}} \right]^{-1} \sigma^{ee(n)}$  with  $e, f = 2$  and 3, be-  
266 cause of the double conditions of eq. (5)



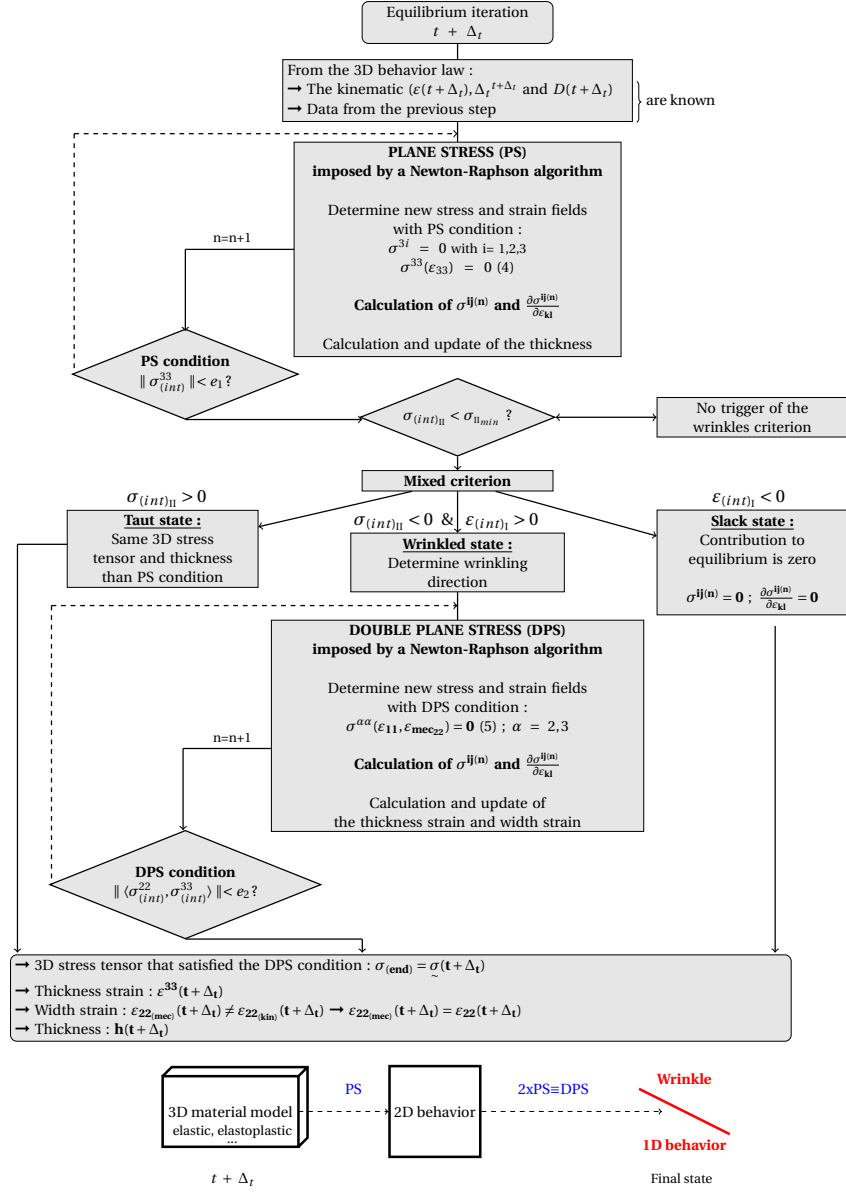


Figure 3: Total algorithm used to model the PS–DPS state with any type of 3D mechanical behaviour.

- 267 (c) then take  $\varepsilon_{ff(n+1)} = \delta\varepsilon_{ff} + \varepsilon_{ff(n)}$  and increment  $n$  as:  $n = n + 1$ ,  
 268 with  $f=2$  and 3  
 269 (d) update the membrane thickness.

270 At the end of the process, after convergence has been reached, which  
 271 is denoted  $\boldsymbol{\sigma}_{(end)}$ , the following data are obtained:

- 272 • the 3D stress tensor  $\boldsymbol{\sigma}_{(end)}$  that satisfies the DPS condition (*i.e.*  
 273 only one value differs from zero:  $\sigma_{(end)}^{11}$ ).
  - 274 • the new thickness strain  $\varepsilon_{33(t+\Delta t)}$  and the new thickness  $h_{(t+\Delta t)}$  of  
 275 the membrane, the transverse mechanical strain  $\varepsilon_{22(t+\Delta t)}$  which is  
 276 noted  $\varepsilon_{22(mec)}$ . The difference between the strain  $\varepsilon_{22(kin)}$  due to the  
 277 kinematic effects and the new  $\varepsilon_{22(mec)}$  is the presence of wrinkles.
- 278 3. as with the PS Newton scheme, in the case of an implicit scheme, the  
 279 tangent behavioural matrix is also calculated based on:  $\frac{\partial \sigma^{11}}{\partial \varepsilon_{11}}$  which  
 280 includes the DPS condition. Details of the calculation of the tangent  
 281 matrix of the DPS condition are given in appendix B.

282 The shape of the wrinkle is not simulated in the PS–DPS model, *i.e.* the  
 283 membrane remains locally plane. The aim of this approach is simply to obtain  
 284 the effects of the wrinkles. In this context, the kinematic deformation  $\varepsilon_{22(kin)}$   
 285 is the global deformation due to the undulation of the wrinkled membrane,  
 286 and the mechanical deformation  $\varepsilon_{22(mec)}$  is the local behaviour of the material  
 287 due to a single tension.  $\varepsilon_{22(kin)}$  could be much higher than  $\varepsilon_{22(mec)}$  and does  
 288 not depend directly on the behaviour of the material, but mainly on the  
 289 intensity of the undulation of the wrinkles, which is responsible of the global  
 290 equilibrium.

291 *Comment 1.* Let us consider a length  $l$  of a membrane strip with a thickness  
 292  $h_0$  and assume that a uniform simple tensile stress is applied along  $\vec{g}_2$  as  
 293 described in fig. 1. This stress makes it possible to obtain a unidirectional  
 294 tensile state. In this case, wrinkles may appear in the direction  $\vec{g}_1$  on the  
 295 membrane. If no condition is imposed in the direction  $\vec{g}_1$ , the mechanical bal-  
 296 ance of the wrinkled membrane will be identical to that of the non-wrinkled  
 297 structure, and it is possible to have the following cases:

- 298 • If the structure remains flat (no wrinkles), the new thickness and the  
 299 width of the membrane will be those corresponding to the initial di-  
 300 mensions modified by the strains required to obtain zero transverse  
 301 stresses.
- 302 • If the structure undulates, the width in the absence of any particular  
 303 conditions along  $\vec{g}_1$  can be arbitrary. In this case, the calculation of the  
 304 tensile force required to achieve the balance of the structure creates an  
 305 issue since the cross section (the thickness and width) can be arbitrary.

306 In this context, two types of thickness have to be considered:

- 307 1. The physical thickness  $h_{(mec)}$  of the undulating membrane. This thick-  
 308 ness will decrease with the tensile stress. In this paper, this thickness  
 309 is also called the mechanical thickness.
- 310 2. The geometric thickness  $h_{(kin)}$ , which is associated with the geometric  
 311 width of the corrugated strip  $l_{(kin)}$  must yield a correct tensile force.

312 The length of the strip  $l$  is identical whether the membrane is wrinkled or  
 313 not. On the other hand, the section of the non-wrinkled membrane given by  
 314 the dimensions  $h_{(mec)} \times l_{(mec)}$  must be identical to the section of the wrinkled

315 membrane  $h_{(kin)} \times l_{(kin)}$ . To obtain an identical volume, it is necessary to  
 316 assume that:

$$h_{(kin)} = \frac{h_{(mec)} \times l_{(mec)}}{l_{(kin)}} \quad (6)$$

317 The geometric thickness will therefore tend to increase when wrinkles are  
 318 present. This finding is described in the numerical shear test presented in  
 319 section 4.1.

320 *Comment 2.* The given precisions  $e_1$  and  $e_2$  may be different. In sections 4  
 321 and 5, for example, the values of these parameters are  $e_1 = e_2 = 1.10^{-3}$ .

322 *Comment 3.* In principle, the PS–DPS model rules out the possibility of  
 323 compressive stresses in the structure. In reality, infinitely small compression  
 324 forces can accumulate in flexible structures, such as the plastic films used  
 325 to make balloons. This admissible compression in the structure depends on  
 326 many parameters such as the nature of the material used and its thickness.  
 327 It can be observed with numerical simulations using shell elements as in the  
 328 validation example tested in section 4.1. In the PS–DPS model, it is also  
 329 possible to leave some compression in the structure by using a parameter  
 330 named:  $\sigma_{\Pi_{min}}$  (see item item 3 of the algorithm in section 2.3). During a  
 331 calculation, if the value of  $\sigma_{(int)\Pi}$  is less than  $\sigma_{\Pi_{min}}$  then the mixed criterion  
 332 is activated and all compressive stresses are eliminated. In the numerical  
 333 examples presented in section 4.1, the value of the admissible compression is  
 334 taken to be a very small value of  $\sigma_{\Pi_{min}} = -1.10^{-15}$ .

335 *Comment 4.* In section 4, several numerical benchmarks will be simulated.  
 336 The PS model presented in section 2.3 will also be compared with the  
 337 PS–DPS model for analysing the effects of wrinkles on the local and global  
 338 equilibrium.

### 339 3. The Dynamic Relaxation method

340 The complexity of the numerical modelling of stratospheric balloons is  
341 due in particular to the lack of flexural rigidity of the membranes and the  
342 occurrence of wrinkles on their surface. During an equilibrium search with  
343 a Newton-Raphson type algorithm, a singular stiffness matrix was obtained.  
344 Various methods such as the use of a numerical viscosity as in the Abaqus  
345 software <49>, for example, have been conventionally used to remove this  
346 singularity. With an implicit approach, it is difficult to accurately model  
347 the deployment phases which occur while the structures are being inflated;  
348 whereas explicit methods are more suitable for dealing with these phases  
349 involving large displacements. On the other hand, these explicit methods  
350 require a large number of computational steps and the final static balancing  
351 of the structure is often very time consuming. For this reason, the Dynamic  
352 Relaxation (DR) method has proven to be useful. This method has the ad-  
353 vantages of the explicit approach while minimizing the computational times  
354 involved. This method, which has also been called pseudo-Dynamic method  
355 <44; 45; 52>, has been used by several authors for the simulations of pres-  
356 surized balloons <40; 53–56> and wrinkling problems <11; 15>.

357 In line with our previous studies <52; 57; 58>, an original DR method was  
358 used here to deal with inflatable structure shape search problems. The main  
359 idea underlying the classical DR methods is that a static solution corresponds  
360 to the limit case of a damped dynamic system. Starting with the fundamental  
361 dynamic equation (eq. (7)), since the mass matrix intervenes only during the  
362 transient phase, the idea is to replace its real value by a fictitious value  
363  $[M']$ , which is optimized with respect to the Courant-Friedrichs-Lewy (CFL)  
364 stability condition <59>.

$$[M'] \{\ddot{X}\} + [C'] \{\dot{X}\} + R(X, \dot{X}) = 0 \quad (7)$$

where  $\{\ddot{X}'\}$ ,  $\{\dot{X}'\}$  and  $\{X\}$  are the acceleration vector, the velocity and the position of nodes, respectively.  $[C']$  is the fictitious viscous damping matrix and  $R(X, \dot{X})$  stands for the residual internal and external forces.  $\{\ddot{X}'\}$  and  $\{\dot{X}'\}$  are regarded fictitious because these terms do not correspond to the real acceleration and the real velocity of the structure.

At convergence, the nodes tend to oscillate around the equilibrium position. The introduction of a damping term thus make it possible to approach the state of static equilibrium. The kinetic or viscous damping have been classically used for this purpose. These two types of damping stabilize the structure in very different ways <58>. In the present study, the kinetic damping method of stabilization, proposed by <44>, with which the overall balance of the structure can be obtained very quickly, was used.

In the case of the kinetic damping, an "undamped" movement is taken to occur with  $[C'] = 0$  and the kinetic energy given in eq. (8) is used:

$$[M']\{\ddot{X}'\} + R(X, \dot{X}) = 0 \quad (8)$$

where the term  $[M']\{\ddot{X}'\}$  is the generalized expression for the acceleration forces.

In the case of a conservative system, the kinetic energy reaches a maximum when the potential energy reaches a minimum. However, a minimum potential energy defines a state closely resembling the state of equilibrium. At each peak in the kinetic energy, the velocities are reset at zero and the computation is relaunched starting at the current position. This process, which consists in freezing the geometrical state of each peak in the kinetic energy, tends to dampen the oscillations. The addition of an artificial damping parameter leads the structure to gradually adopt a statically balanced form. The condition for stopping the calculation is defined by a fixed parameter, named  $\varepsilon_{DR}$ , which corresponds to the equilibrium state of the structure.

391 This parameter is calculated using the relation:

$$\max \left( \frac{\| \text{Residual static} \|_{\infty}}{\| \text{Reactions} \|_{\infty}}, \frac{\text{Kinetic energy}}{\text{Internal energy}} \right) \leq \varepsilon_{DR} \quad (9)$$

392 *Comment.* In section 4, the precision is set at  $\varepsilon_{DR} = 1.10^{-4}$  which makes it  
 393 possible to make novel comparisons with data in the literature. In section 5, a  
 394 numerical test on the inflation of a stratospheric balloon is performed with the  
 395 PS–DPS model and a non-linear behavioural law. In this case, the precision  
 396 is set at  $\varepsilon_{DR} = 5.10^{-3}$ . This value is currently used by the CNES in all their  
 397 balloon simulations because it gives precise local and global equilibria.

398 To solve the time problem, the method used here is based on the explicit  
 399 Centered Finite Differences (CFD) method. The flow of the process is controlled by a fictitious time with an increment which is arbitrarily set at 1.  
 400 The fictitious mass matrix is sized so as to satisfy the stability condition of  
 401 eq. (10) more closely. For this purpose, a mass matrix calculated from the effective stiffness matrix is used, based on the Gershgorin theorem <45>. The  
 402 mass matrix is updated only at specific times: at the start of the calculation  
 403 and possibly after a damping step, which limits the time required to perform  
 404 the computation. The mass matrix is calculated here only at the beginning  
 405 of the simulation, taking:

$$m_i = \frac{\lambda \Delta t'^2}{2} S_i \rightarrow S_i = \sum_j |K_{ij}| \quad (10)$$

408 where  $m_i$  is the mass at node  $i$ ,  $\Delta t'$  is the fictitious time,  $S_i$  is calculated  
 409 from the matrix  $K_{ij}$  which is the local stiffness matrix of each elements.  $S_i$   
 410 is calculated by taking the maximum value of the sum of the absolute values  
 411 of the stiffness along the three axes of the Cartesian coordinate system. This  
 412 maximum is applied in all the three directions. An increase occurs in the  
 413 three eigenvalues obtained via the Gershgorin theorem applied locally to

each matrix [45](#).  $\lambda$  is an adjustable parameter used to compensate for the instability of the schema resulting, for example, to the approximation of Gershgorin's theorem.

## 4. Numerical experiments

To investigate the performances of the present wrinkling model, several numerical benchmarks are modelled here and compared with data presented in literature.

First, by reproducing shear and torsion tests, structures subjected to in-plane loading are studied. The deployment of a square cushion is then carried out in order to test the validity of the model on a structure resembling that of stratospheric balloons. These complementary tests have been frequently used in previous studies on wrinkling models. In some cases, the membrane shifts locally from a wrinkled to a taut state (in torsion and cushion tests). In other cases, the membrane is completely wrinkled (either in one direction or in all directions), as in shear tests. In shear and torsion tests, an isotropic elastic law is used, and these tests are carried out under small strains, as performed in literature. In the case of the inflation of a square cushion, finite strains and elastic behaviour are first tested, but a hyperelastic model is then used to analyse the responses of the PS–DPS model with this non-linear behaviour.

### 4.1. Rectangular membrane under shear loading

A two-dimensional rectangular membrane under shear loading was first tested. This test has been widely used in the literature [3](#); [4](#); [6](#); [17](#); [60–62](#). The solutions obtained with the PS and PS–DPS models were compared with numerical and experimental results previously obtained with an elastic law.



439 The geometry, loading conditions and material parameters used in this  
 440 shear test are presented in fig. 4. A 0.025 mm thick 2D rectangular mem-  
 441 brane (the plane of the membrane) measuring 380 mm x 128 mm in the  $XY$   
 442 plane was fixed at the lower edge, while the upper edge could move only in  
 443 the horizontal direction. The geometry was meshed with 300 linear triangu-  
 444 lar membrane elements. These elements include one Gauss point and finite  
 445 transformations (*i.e.* large displacements and deformations) were taken into  
 446 account. The parameters  $\lambda$  used in the DR method were set at 2.

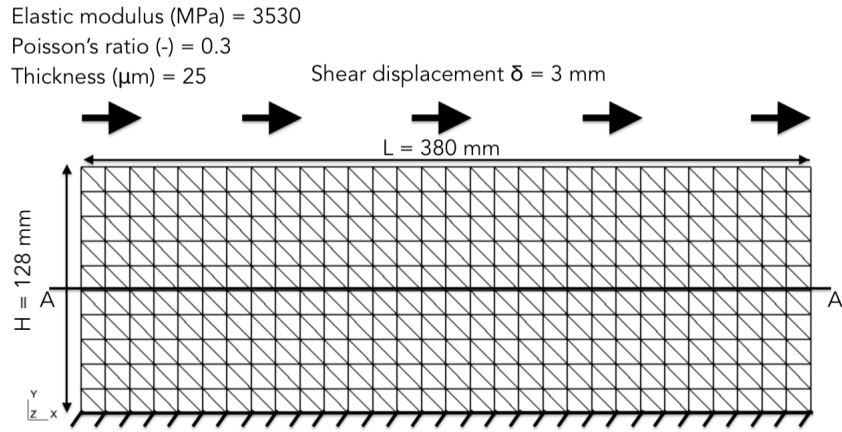


Figure 4: Membrane properties and kinematic boundary conditions in shear test with 300 linear triangular membrane elements performed with the PS and the PS–DPS models.

447 The flat membrane was loaded with a prestress with a magnitude of 1.5  
 448 N/mm<sup>2</sup> in the  $Y$ –direction to introduce an initial stiffness. The prestress  
 449 was then held constant while the upper edge was gradually moved in the  
 450 horizontal direction until this movement had covered a distance of +3 mm  
 451 (see fig. 4).

452 In order to compare our results with data in the literature, this test was  
 453 also simulated with shell elements in Abaqus <49> using the same method  
 454 presented by Wong and Pellegrino in <3>. In this case, this simulation was

455 performed by taking 3960 S4R5 shell elements. As with membrane elements  
 456 in Herezh++, a  $1.5 \text{ N/mm}^2$  prestress was prescribed on the upper side of  
 457 the rectangular membrane in order to induce an initial stiffness. After cal-  
 458 culating the first buckling modes, the out-of-plane displacements caused by  
 459 these modes were imposed like imperfections in addition to the boundary  
 460 conditions of displacement of 3 mm in the  $X$ -direction. If the shell mesh is  
 461 sufficiently fine, this method gives the shape of the wrinkles and eliminates  
 462 the compression stresses due to the wrinkles.

463 The shear forces applied to the membrane using the PS, PS-DPS and  
 464 shell models are presented and compared in fig. 5a as a function of the shear  
 displacement.

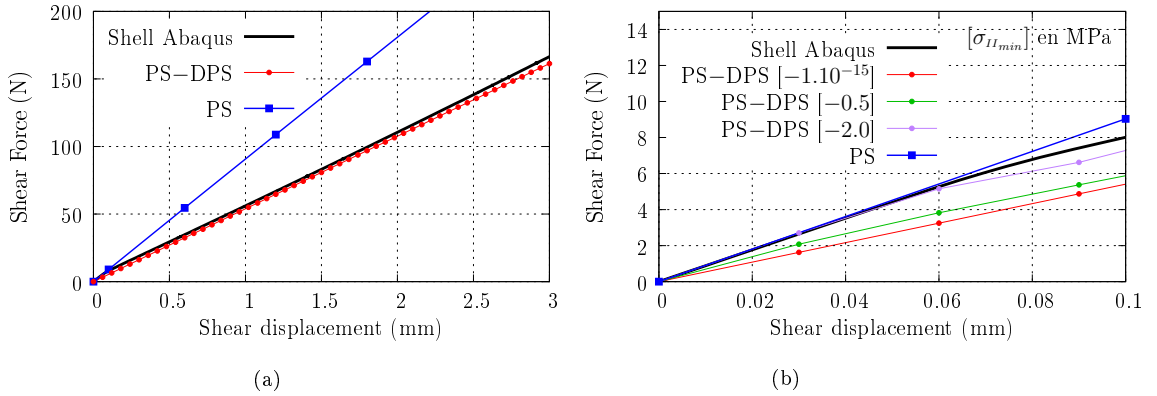


Figure 5: (a) Comparison of shear force/displacement relationships obtained using the shell model, the classical PS membrane model and the PS-DPS wrinkle model. (b) Zoom of the beginning of the shear force/displacement relationship showing the influence of the compressive stress  $\sigma_{II_{min}}$  (indicated in brackets) used in the PS-DPS model.

465

466 The initial in-plane shear stiffness of the shell model is approximately  
 467 equal to  $101 \text{ N/mm}$ , which corresponds to the value given by Wong and  
 468 Pellegrino. This stiffness obtained with the shell model decreases quickly  
 469 at a value of  $55 \text{ N/mm}$ , showing a similar trend to that observed with the

470 PS–DPS model. This loss of stiffness is due to the development of wrin-  
 471 kles on the structure <3>. The PS membrane model does not account for  
 472 the softening associated with the formation of wrinkles. Contrary to what  
 473 occurs with the shell model, the relationship between force and displace-  
 474 ment remains linear with the PS–DPS model, with which no compression  
 475 by default can be included in its formulation. However, as explained in the  
 476 Comment 3 in section 2.4, it is possible in the PS–DPS model to control the  
 477 compressive stress state with the parameter  $\sigma_{IImin}$ . Figure 5b shows the influ-  
 478 ence of the compressive stress parameter  $\sigma_{IImin}$  on the initial stiffness at the  
 479 beginning of the shear-displacement curve. By default, this value was set at  
 480  $-1.10^{-15}$  MPa and in this case, during the initiation of buckling, the stiffness  
 481 remains linear, contrary to what is predicted by the shell model. When this  
 482 compression stress value is increased to almost 2 MPa, the PS–DPS model  
 483 is then reflect the initial decrease in the stiffness, as observed with the shell  
 484 model used by Wong and Pellegrino.

485 The principal stresses  $\sigma_I$  and  $\sigma_{II}$  across the middle of the membrane (see  
 486 cross section A-A in fig. 4) are plotted in fig. 6a. This distribution of the prin-  
 487 cipal stresses is compared with that obtained with the Abaqus shell model  
 488 using 3960 S4R5 elements, the membrane model proposed by Deng and Pele-  
 489 grino <38> and the PS–DPS model. The PS–DPS model gives results  
 490 which are consistent with the Abaqus shell solution and the membrane wrin-  
 491 kling model previously studied in the literature. The minor principal stress  
 492  $\sigma_{II}$  is null in all these cases.

493 According to Deng and Pellegrino <38>, the orientation of wrinkles is  
 494 equal to  $45^\circ$  at the centre of the membrane. The major principal strain  $\varepsilon_I$   
 495 and the major principal stress  $\sigma_I$  are exerted in the same direction as the

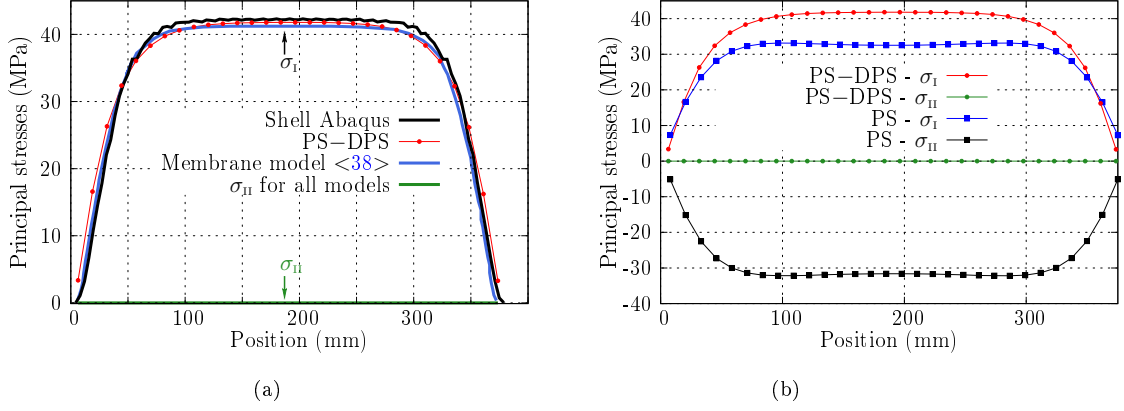


Figure 6: (a) Distribution of the principal stresses  $\sigma_I$  and  $\sigma_{II}$  along the middle of the membrane for the Abaqus shell model, the membrane model presented in <38> and the PS-DPS model. (b) Comparison of these stresses between our PS membrane model and the PS-DPS model.

496 wrinkles. The following equations can be used to determine  $\sigma_I$  in this region:

$$\varepsilon_I = \frac{\lambda}{2} \text{ and } \sigma_I = E \times \varepsilon_I \quad (11)$$

497 where  $\lambda = \frac{\delta}{H}$  is the elongation along  $X$ ,  $\delta$  is the horizontal displacement  
 498 imposed,  $H$  is the height of the membrane (see fig. 4) and  $E$  is the Young's  
 499 modulus.

500 Based on these equations, Wong and Pellegrino <63> have established  
 501 that this major principal stress, is equal to 41.37 MPa. With the PS-DPS  
 502 model, a value of 41.79 MPa is obtained, amounting to a difference of 1%.  
 503 Figure 6b gives the major and minor principal stresses obtained with the PS  
 504 and PS-DPS models in order to show the impact of the wrinkles on the local  
 505 equilibrium of the structure. With the PS model, the major principal stress  
 506  $\sigma_I$  is lower than in the PS-DPS model, giving a difference of 20.7% and a  
 507 minor principal stress of  $\sigma_{II} \approx -30$  MPa is obtained. This value of  $\sigma_{II}$  was  
 508 also obtained by Jarasjarungkiat et al. <19> with a classical PS membrane  
 509 model.

As described in section 2.4, the PS–DPS model makes it possible to account for the wrinkles in a membrane structure without modelling the out-of-plane displacement. The mechanical strain that the structure actually undergoes is different from the geometric strain caused by the wrinkles. As mentioned above, the geometrical thickness  $h_{(kin)}$  is due to the presence of wrinkles and the mechanical thickness  $h_{(mec)}$  is equivalent to the physical thickness. The mechanical and the geometrical thicknesses obtained along the section of the membrane at the end of the shear test are compared in fig. 7.

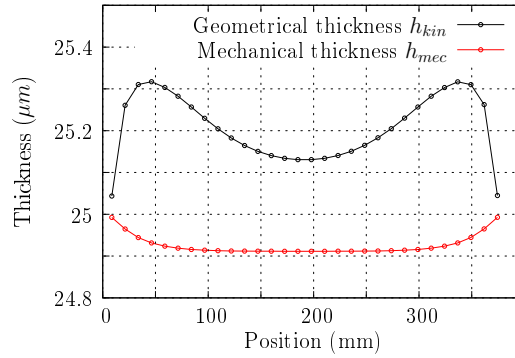


Figure 7: Distribution of the geometrical thickness  $h_{(kin)}$  and the mechanical thickness  $h_{(mec)}$  along the middle of the membrane in the case of the PS–DPS model.

The geometrical thickness  $h_{(kin)}$  increases in the wrinkled area due to the out-of-plane movement caused by the formation of the wrinkles, whereas the mechanical thickness is negative because the membrane is in a uniaxial tensile state. The distribution of geometric thickness consists of two high peaks ( $h_{(kin)} \approx 25.3 \mu m$ ) located near the free edges on both sides of the membrane. The geometrical thickness decreases in the middle of the membrane, but it is still greater than the initial thickness ( $h_{(kin)} \approx 25.1 \mu m$ ). Similar results were obtained experimentally by Wong et al. <62> in a study in which they subjected a rectangular membrane to a state of simple shear. These authors

528 reported that the out-of-plane deflection was greater near to the free edges  
529 on both sides of the membrane. In the middle, the out-of-plane displacement  
530 decreased and the region was characterised by fairly uniform wrinkles.

531 To conclude this part, although the PS–DPS model is not suitable for  
532 modelling the shape of wrinkles, the geometrical thickness is a good indica-  
533 tion to the wrinkling pattern in the membrane. This shear test was the first  
534 step in the validation of the PS–DPS wrinkle model. The torsion test which  
535 will now be described was performed in order to analyse the response of the  
536 PS–DPS model under these new loading conditions with an elastic law.

#### 537 4.2. Torsion test on an annular membrane

538 In this numerical test, an annular membrane is attached to a rigid hub  
539 along the inner edge and to a guard ring along the outer edge as shown in  
540 fig. 8. The rotation of the rigid disc causes wrinkling of the membrane <12>.  
541 Two tests, classically used in the literature, are simulated: the first is a torsion  
542 test without any initial prestress <4; 19> and an initial prestress is added in  
543 the second test <7; 27>. In both cases, an analytical solution is presented  
544 in <64> and theses solutions are also obtained with a Python script. In the  
545 case of the prestress torsion test, the membrane shifts locally from a one-  
546 directional wrinkled state to a stretched state (devoid of wrinkles). The aim  
547 of this prestress torsion test is to determine the robustness of the PS–DPS  
548 model when moving from one state to another. The value of parameter  $\lambda$   
549 adopted in the DR method was set at 4 in all these torsion tests.

##### 550 4.2.1. Torsion without any prestress

551 In this test, all translations of the outer nodes are fully constrained and  
552 the inner rigid disk is rotated clockwise by the angle  $\theta$  (see fig. 8). The mesh is  
553 composed of 180 quadrangular membrane elements with linear interpolation.

Elastic modulus (Pa) =  $10^5$   
Poisson's ratio (-) = 0.45  
Thickness (m) = 1.0

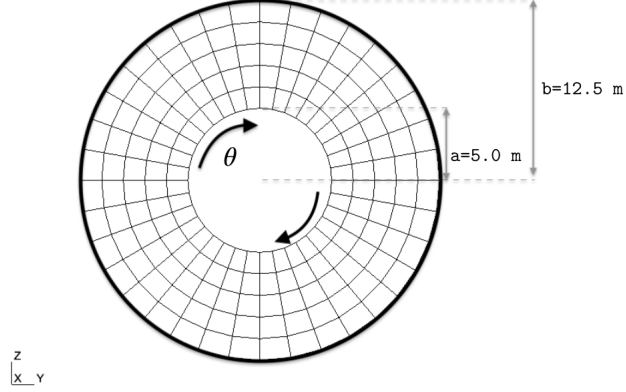


Figure 8: Geometry, physical properties and load at the inner edge of the annular membrane.

554 These elements include four Gauss points and involve finite transformations  
555 (*i.e.* large displacements and deformations). The dimensions and loading  
556 conditions of the membrane studied here are given in fig. 8 as well as the  
557 properties of the linear elastic law used.

558 In the studies by Jarasjarungkiat et al. <4; 19>, the angle  $\theta$  imposed  
559 on the inner rigid disk is  $10^\circ$ . However, with this angle, the strain values  
560 obtained are significantly greater than 10% which results relatively large  
561 strains. As explained above in the Introduction, the PS–DPS model involves  
562 the Almansi strain measure whereas in literature, the Green strain measure  
563 has been generally used so far with wrinkle models. As shown in fig. 9, the  
564 directions of the major principal stresses are nevertheless compatible with  
565 those reported in <12; 65> with an angle of  $10^\circ$ . In order to compare the  
566 numerical results obtained with the PS–DPS model and data presented in  
567 previous numerical studies, an analytical solution given by Mikulas <64>

568 in the case of small deformations was used with an angle of  $0.728^\circ$ , which  
 569 corresponds to a moment equal to  $10^5 \text{N.m}$ . This small angle makes it possible  
 570 to compare data obtained in the case of small rotations with strain fields of  
 571 less than 10%.

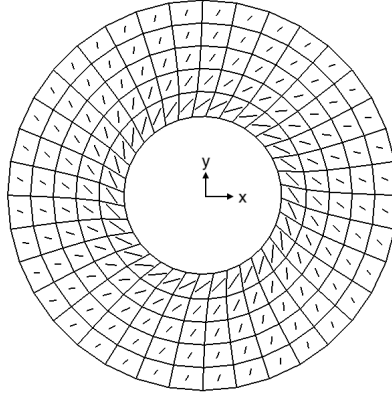


Figure 9: Deformed mesh with representation of the principal stress vectors involving an angle  $\theta = 10^\circ$  in the case of a linear elastic material.

572 In this case, wrinkling occurs over the entire membrane as soon as an  
 573 angle is applied to the hub. Based on equations given in <64>, it is possible  
 574 to compute the stress state in the membrane in two steps.

575 The first step consists in determining the value of the constant  $C_2$  which  
 576 satisfies the boundary conditions on the edges of the membrane, according  
 577 to the following equation:

$$\frac{1}{\frac{4\pi^2 t^2 C_2^2 a^2}{M^2} - 1} + \log\left(\frac{4\pi^2 t^2 C_2^2 a^2}{M^2} - 1\right) - \frac{1}{\frac{4\pi^2 t^2 C_2^2 b^2}{M^2} - 1} - \log\left(\frac{4\pi^2 t^2 C_2^2 b^2}{M^2} - 1\right) = 0 \quad (12)$$

578 where  $a$  is the inner radius,  $b$  is the outer radius,  $t$  is the membrane thickness  
 579 and  $M$  is the torque applied.

580 When the constant  $C_2$  is known, the second step consists in calculating



the radial  $\sigma_r$  and tangential stresses  $\sigma_\theta$  based on the following equations:

$$\begin{cases} \sigma_r = \frac{1}{r} \sqrt{C_2 - \frac{M^2}{4\pi^2 t^2 r^2}} \\ \sigma_\theta = \frac{M^2}{4\pi^2 t^2 r^4} \frac{1}{\sigma_r} \end{cases} \quad (13)$$

where  $r$  is the radial position in the membrane.

To determine the angle of the wrinkles  $\alpha$ , as shown in fig. 10, the stress field can be written as follows:

$$\begin{cases} \alpha = \arcsin \left( \frac{M}{2\pi t \sqrt{C_2} r} \right) \\ \sigma_I = \frac{\sigma_r}{\cos^2 \alpha} = \frac{\sigma_\theta}{\sin^2 \alpha} \end{cases} \quad (14)$$

This same problem has been solved using TF theory by Reissner <66>, who established that the tension lines start from the inner edge, and because of the symmetry, each of these lines forms along the inner edge the same angle with the radius from the origin (fig. 10).

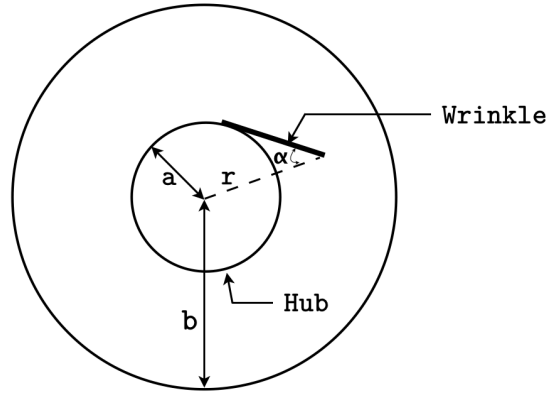


Figure 10: Angles of wrinkles  $\alpha$  as described in <64>.

One simulation was performed with the PS–DPS model with an angle  $\theta$  equal to  $0.728^\circ$  and compared with this analytical solution, as shown in fig. 11. The results show the evolution of the major principal stress  $\sigma_I$  along

the radius of the structure. The PS–DPS model predicts the same evolution of the decrease of the principal stress along the radius as the analytical solution. The PS–DPS model can be used to simulate a completely wrinkled membrane state. The next test consists in adding an initial prestress to the torsion test.

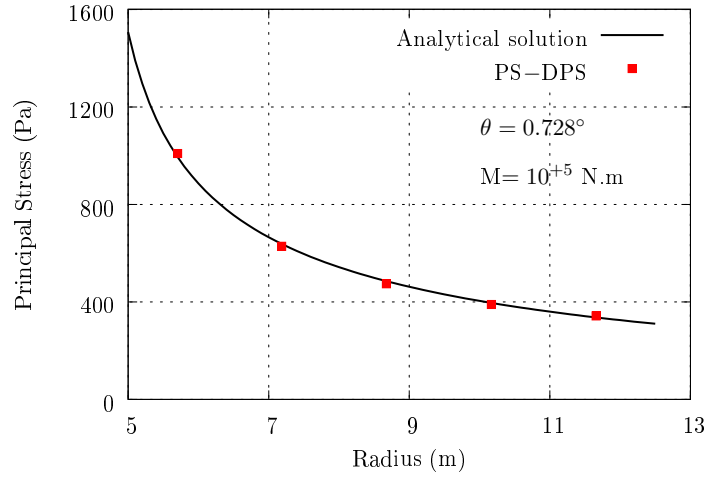


Figure 11: Comparison between the results obtained with the analytical model <64> and the PS–DPS model on the evolution of the major principal stress  $\sigma_1$  with  $\theta = 0.728^\circ$  and 180 quadrangular membrane elements.

596

#### 597 4.2.2. Torsion with prestress

598 The rigid hub was then subjected to a torque loading  $M$  and rotated  
599 through an angle  $\phi$ , and this membrane was subjected to a uniform prestress  
600  $\sigma_0$ . The geometric and elastic material parameters used in this test are  
601 presented in fig. 12a.

602 When the torsion loading was applied by increasing the moment  $M$ , wrin-  
603 kles began to form around the hub up to some radius  $R$ , as explained for  
604 example by Akita et al. <27>. The two meshes, described in fig. 12b, with  
605 quadrangular membrane elements, with linear interpolation and four Gauss

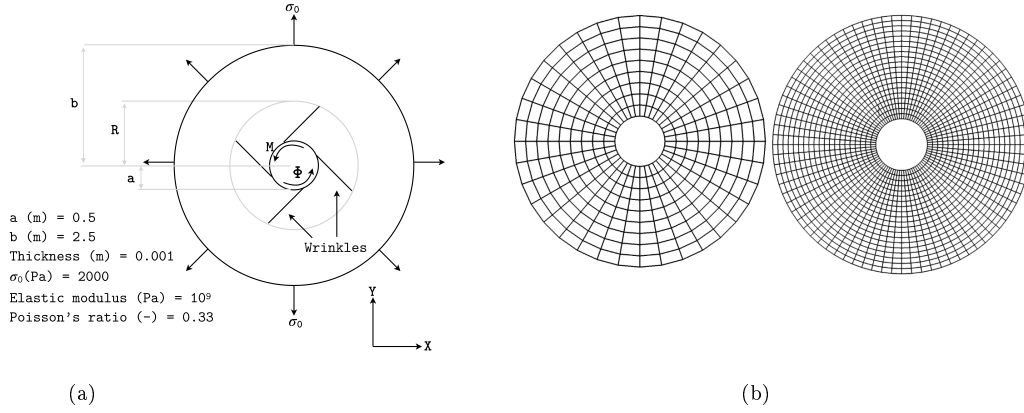


Figure 12: **a)** Dimensions and material properties in the annular membrane test under torque applied to the inner edge with prestress  $\sigma_0$ . **b)** Coarse (324 elements) and fine (1600 elements) meshes used to simulate this test.

points, are tested in order to determine the influence of the finite element size. The coarse mesh was composed here of 324 elements and the fine mesh, of 1600 elements.

The analytical solution of this problem presented in <64; 67> has been used by several authors <27; 68>. In this analytical solution, the relation between the wrinkle radius  $R$  and the moment  $M$  is given by the following equations. The quadratic eq. (15) has to be solved to determine the constant  $C_1$ . This constant  $C_1$  can be used to calculate  $C_2$  with eq. (16). Lastly, we checked the values of this constant with eq. (17).

$$C_1^2 - \left[ 1 + 2C_1 \left( \frac{a^2}{b} \right) \right]^2 \bar{R}^4 + \bar{M}^2 = 0 \quad (15)$$

$$C_2 = (\bar{R} + [\frac{1}{\bar{R}} + 2\bar{R}\frac{a^2}{b}])C_1^2 + (\frac{\bar{M}}{\bar{R}})^2 \quad (16)$$

$$\frac{1}{A} + \frac{1}{B} - \ln(\frac{B}{A}) - \frac{2}{3} = 0 \quad (17)$$

615 where  $\overline{M} = \frac{M}{2\Pi\sigma_0 t a^2}$  ;  $A = \frac{C_2}{\overline{M}^2} - 1$  ;  $B = \overline{R}^2 \frac{C_2}{\overline{M}^2} - 1$  in which  $\overline{R} = \frac{R}{a}$ ,  
 616  $R$  being the radial extent of the wrinkled region,  $C_1$  and  $C_2$  are constants  
 617 which can be used to calculate the stress field,  $t$  is the thickness of the film  
 618 and  $a$  and  $b$  are the inner and outer radii, respectively.

619 The relation between the moment  $M$  and the twist angle  $\phi$  is given by:

$$\overline{\phi} = \frac{3\overline{M}}{8(1 - \frac{a^2}{b^2})} \left[ \frac{\frac{1}{\overline{R}^2} - 1}{B} + \ln\left(\frac{B}{A}\right) + \frac{1}{\overline{R}^2} - \frac{8}{3} \left(\frac{a^2}{b^2}\right) + \frac{5}{3} \right] \quad (18)$$

620 where:

$$\phi = \frac{4\overline{\phi}\sigma_0 \left(1 - \frac{a^2}{b^2}\right)}{3E} \quad (19)$$

621 In the simulation, the angle  $\phi$  determined by eq. (19) is imposed on the  
 622 inner radius  $a$ .

623 The moment applied causes the occurrence of wrinkles on a certain radius  
 624 denoted  $\overline{R}$ . Contrary to the torsion test without any prestress presented in  
 625 section 4.2.1, the structure falls into two areas. With values of  $\overline{R}=1.2, 1.4$   
 626 and  $1.6$ , the membrane is in a wrinkled state in one direction and beyond  
 627 these values, the membrane is stretched. Comparisons are made here only  
 628 with these values of  $\overline{R}$ .

629 After solving the previous equations, the ratios  $\frac{\sigma_I}{\sigma_0}$  and  $\frac{\sigma_{II}}{\sigma_0}$  between the  
 630 principal stresses and the prestress (with  $\sigma_I > \sigma_{II}$ ) are given in the wrinkled  
 631 zone  $\bar{r} < \overline{R}$  according to the following relations:

$$\begin{cases} \frac{\sigma_I}{\sigma_0} = \frac{\frac{C_2}{\bar{r}}}{\sqrt{C_2 - \frac{\overline{M}^2}{\bar{r}^2}}} \\ \frac{\sigma_{II}}{\sigma_0} = 0 \end{cases} \quad (20)$$

632 where  $\bar{r} = \frac{r}{a}$ .

These ratios are obtained in the wrinkle-free zone ( $\bar{r} \geq \bar{R}$ ), where:

$$\begin{cases} \frac{\sigma_I}{\sigma_0} = 2C_1 \frac{a^2}{b^2} + 1 + \sqrt{\frac{C_1^2 + \bar{M}^2}{\bar{r}^2}} \\ \frac{\sigma_{II}}{\sigma_0} = 2C_1 \frac{a^2}{b^2} + 1 - \sqrt{\frac{C_1^2 + \bar{M}^2}{\bar{r}^2}} \end{cases} \quad (21)$$

Figs. 13a to 14b give the ratios  $\frac{\sigma_I}{\sigma_0}$  and  $\frac{\sigma_{II}}{\sigma_0}$  as a function of  $\bar{r} = \frac{r}{a}$ , respectively, with various torques values in the case of coarse and fine meshes.

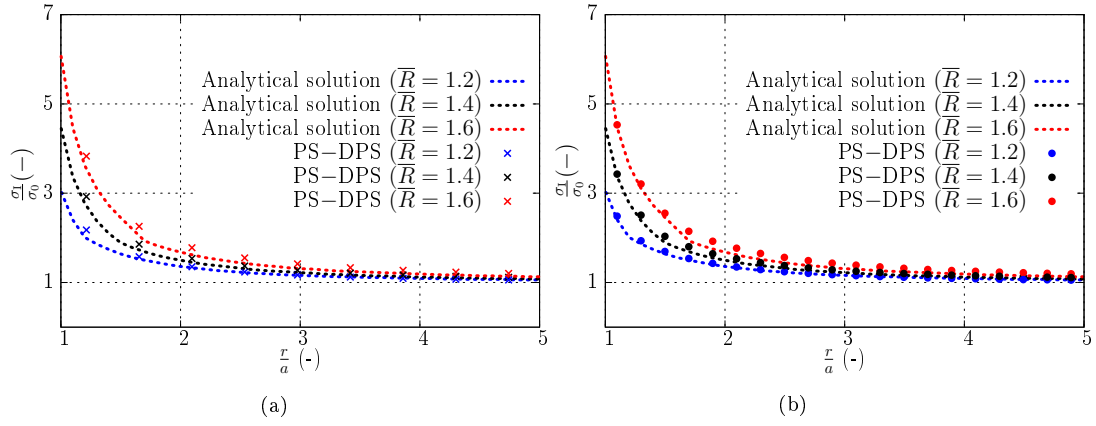


Figure 13: Comparison between the analytical solution and the results obtained with the PS-DPS model for  $\frac{\sigma_I}{\sigma_0}$ , depending of the radial position  $\frac{r}{a}$ . (a) Coarse mesh (324 elements). (b) Fine mesh (1600 elements).

The switch between the wrinkled area and the stretched area is shown in fig. 14. The ratio  $\frac{\sigma_{II}}{\sigma_0}$  is equal to zero when the structure is wrinkled, but increases along the radius in the stretched area. Figure 13 shows that the evolution of  $\frac{\sigma_I}{\sigma_0}$  is accurately predicted by the PS-DPS model with both coarse and fine meshes. However, in the case of the evolution of  $\frac{\sigma_{II}}{\sigma_0}$ , the solution obtained with the fine mesh resembles the analytical solution slightly more closely than that obtained with the coarse mesh. In fact, the influence of the mesh is quite weak on the results of this test with the PS-DPS model. The

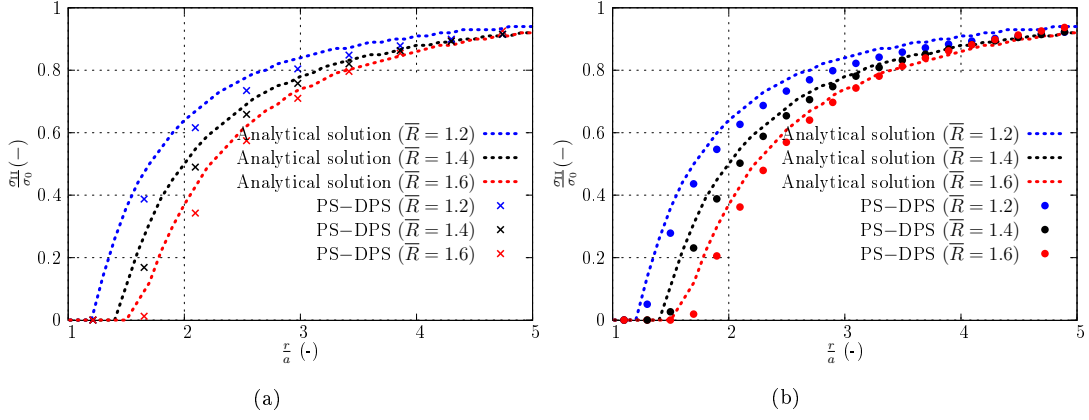


Figure 14: Comparison between the analytical solution and the results obtained with the PS–DPS model for  $\frac{\sigma_{II}}{\sigma_0}$ , depending of the radial position  $\frac{r}{a}$ . (a) Coarse mesh (324 elements). (b) Fine mesh (1600 elements).

645 results here resemble the analytical solutions, even with a mesh composed of  
 646 only a few elements, which is not the case with a shell mesh, as observed in  
 647 the shear test presented in section 4.1.

#### 648 4.3. Inflation of a square cushion with an elastic law

649 In this example, the efficiency of the PS–DPS model is tested in the case  
 650 of an inflatable structure. This test has been extensively studied with an elas-  
 651 tic law in the literature <4; 19; 20; 35; 43>. It consists in gradually inflating  
 652 a flat square elastic isotropic membrane, increasing the constant pressure up  
 653 to 5 kPa. The material properties and dimensions of the undeformed cushion  
 654 are given in fig. 15.

655 By applying appropriate boundary conditions in the horizontal mid-plane,  
 656 it is only necessary to model one upper quarter of the cushion. This eighth  
 657 of the square cushion was simulated with various mesh sizes. The initial  
 658 discretization was  $4 \times 4$  and refined as  $5 \times 5$ ,  $8 \times 8$  and  $10 \times 10$  quadrangular  
 659 elements with linear interpolation and 4 Gauss points, consecutively. Figs

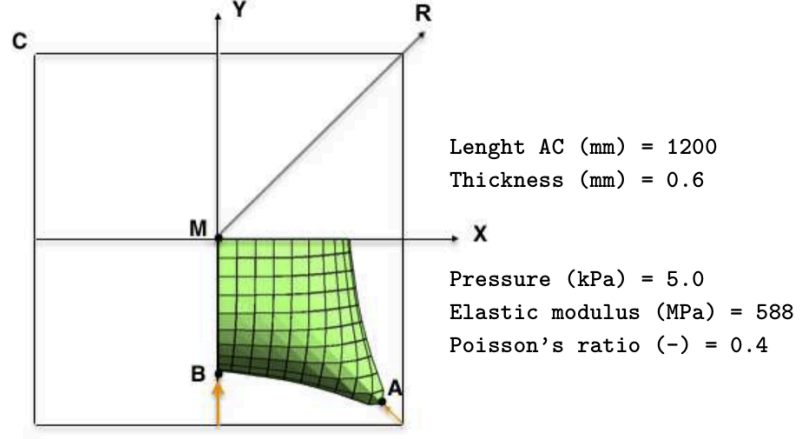


Figure 15: Membrane geometry and material properties of the inflated square cushion test.

660 16a and 16b show the deformed mesh given by the PS–DPS and PS models,  
 661 respectively (showing the symmetrical parts of the meshes). The parameter  $\lambda$  used in the DR method was set in this case at 1.5.

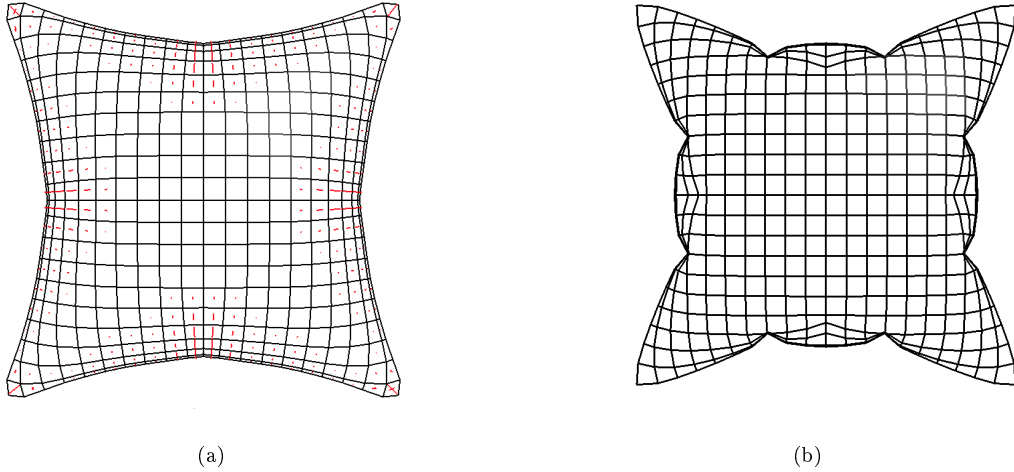


Figure 16: Deformed shape of the inflated square cushion testes at a pressure of 5 kPa with a mesh consisting of  $5 \times 5$  elements. (a) With the PS–DPS model showing the wrinkled zones (in red). (b) With the PS model without taking the wrinkles into account.

662

663 Previous authors have compared four quantities: the distribution of the  
 664 stresses along in the direction  $X$ , the major principal stress and the vertical  
 665 displacement occurring in the centre  $M$  and the displacement in the direction  
 666  $Y$  at point  $B$  (see fig. 15). The results obtained with PS–DPS model were

667 compared with data previously published in the literature <4; 19; 20; 35; 43>  
668 and simulations performed using the "No compression" model implemented  
669 in Abaqus. This model approaches the elastic behaviour by first solving for  
670 the principal stresses assuming linear elasticity and then setting the appro-  
671 priate principal stress values to zero. The associated stiffness matrix compo-  
672 nents were also set at zero. "No compression" model can be rather unstable,  
673 which explains why convergence problems are liable to occur.

674 In figs 17a and 17b, data obtained in previous studies and those obtained  
675 with the PS–DPS model are compared in terms of the displacement of points  
676  $M$  and  $B$ . The results obtained with the PS–DPS model are almost identical  
677 to those obtained with the models presented in <4; 19; 20; 35; 43>. These  
678 figures show that the shape of the cushion is accurately predicted at points  $M$   
679 (in the stretched area) and  $B$  (in the wrinkled area) by the PS–DPS model.  
680 Note that the "No compression" Abaqus model gives strange displacements  
681 at point  $B$  in the wrinkled area, as previously reported by Contri and Schre-  
682 fler <35>. These models involve the used of a static implicit scheme to solve  
683 the wrinkling problem. An equilibrium position of the membrane is first de-  
684 termined with active compressive stresses and tensile stresses. If at least one  
685 such principal stress is found to be compressive in an element, a new stress  
686 state with only the tensile stresses active is obtained. These models do not  
687 seem to be as effective as the PS–DPS model.

688 In fig. 18a, the major principal stress  $\sigma_1$  occuring at point  $M$ , depending  
689 of the mesh size used, is compared with results obtained in <19; 43>. The  
690 stress states predicted with the PS–DPS model show good agreement with  
691 these previous data. Figure 18b shows the evolution of the stresses  $\sigma_{11}$  and  
692  $\sigma_{22}$  in the direction  $X$  in the cushion predicted by the PS–DPS model and  
693 the membrane model presented by Lee et al. <11>, in the only study in



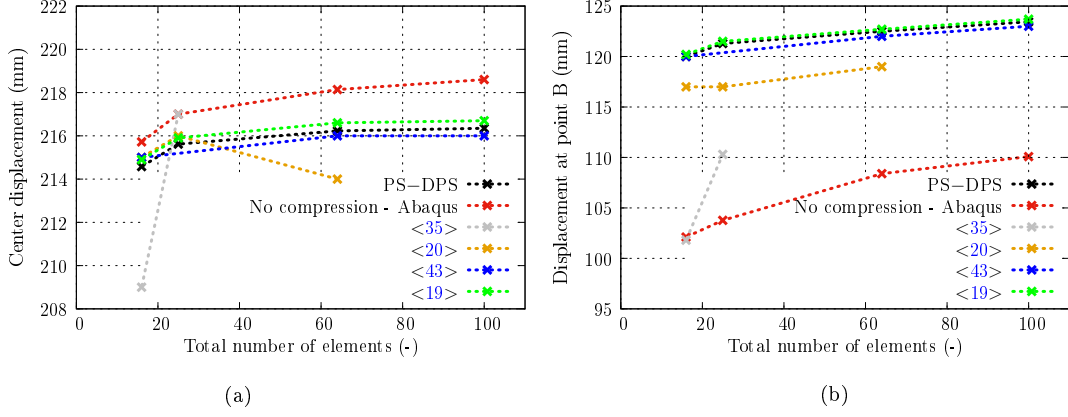


Figure 17: Displacement at the centre (point  $M$ ) (a) and point  $B$  (b) predicted with various mesh sizes ( $4 \times 4$ ,  $5 \times 5$ ,  $8 \times 8$  and  $10 \times 10$  elements) in comparison with data obtained in <4; 19; 35; 43>, the "No compression" model and the PS–DPS model.

the literature to deal with this evolution. The results give a picture of the wrinkling behaviour and the tensile area in the cushion.  $\sigma_{22}$  is equal to zero and  $\sigma_{11}$  is almost equal to 1.5 MPa in the wrinkled area. In the taut area, the values of  $\sigma_{22}$  and  $\sigma_{11}$  both increase. The values of  $\sigma_{22}$  and  $\sigma_{11}$  are equal in the centre of the cushion (position  $\approx 25$  mm). The stress field predicted with the PS–DPS model is similar to that obtained in previous studies.

This test finishes the validation section of the PS–DPS model with a linear elastic law in comparison with literature cases. These previous tests showed the ability of the PS–DPS model to account for the formation of wrinkles in flexible structures. The tests described in the next section were performed on the PS–DPS model with a non linear law in order to determine the effects of the mechanical behaviour on the shape of the cushion and the local equilibrium.

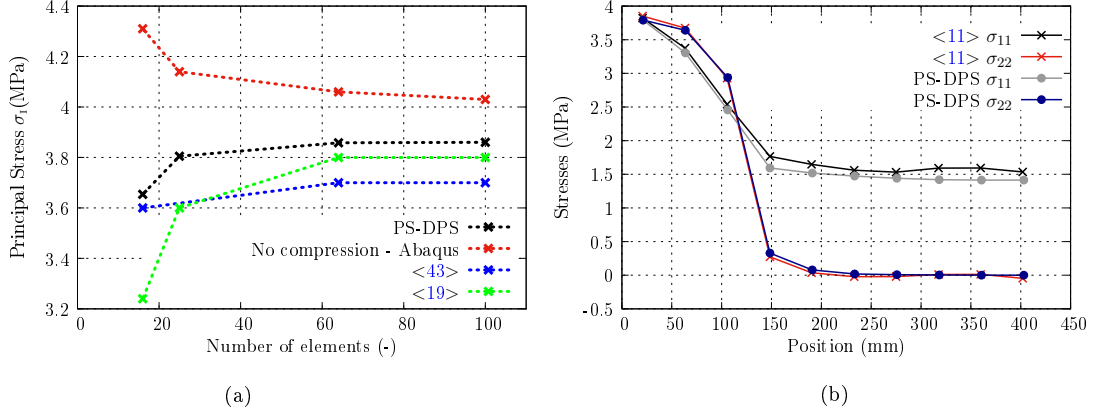


Figure 18: (a) Major principal stress  $\sigma_1$  at point  $M$  with meshes consisting of  $4 \times 4$ ,  $5 \times 5$ ,  $8 \times 8$  and  $10 \times 10$  elements in comparison with data presented in previous studies <19> <43>, the "No compression" model and the PS–DPS model. (b) Comparison between the stresses  $\sigma_{11}$  and  $\sigma_{22}$  occurring in the  $X$  direction of the cushion obtained in <11> and with the PS–DPS model.

#### 707 4.4. Inflation of a square cushion with a non-linear law

708 Stratospheric balloons are made of very fine plastic films showing complex  
 709 mechanical behaviour. In order to approach this non linear behaviour, a  
 710 simulation was performed on the inflation of a square cushion using the  
 711 PS–DPS model and the original hyperelastic law initially defined by Favier  
 712 et al. <69>. This hyperelastic part was previously used in a study of Zrida  
 713 et al. <70> to simulate the behaviour of polymers.

714 The hyperelastic potential  $W$  involved in this law was defined on the basis  
 715 of four material parameters, using the invariants of the Almansi measure  $\epsilon$   
 716 according to the relation:

$$W = \frac{K}{6} \ln^2(V) + \frac{Q_{0r}^2}{2\mu_0} \ln \left( \cosh \left( \frac{2\mu_0 Q_\epsilon}{Q_{0r}^2} \right) \right) + \mu_\infty Q_\epsilon^2 \quad (22)$$

717 where in the case of a shear test,  $\mu_\infty$  denotes the final slope of the stress  
 718  $\tau$ -strain  $\gamma$  curve,  $\mu_0 + \mu_\infty$  denotes the initial slope  $\tau$  versus  $\gamma$  and  $Q_{0r}$  stands

719 for the level of the final tangent to the curve (*i.e.* the intersection between  
 720 the final tangent and the vertical stress axis) (for details of these material  
 721 parameters, see fig. 19).  $K$  is the bulk modulus, on which the changes in  
 722 volume mainly depend.  $V$  stands here for the relative changes in volume and  
 723  $Q_\varepsilon$  denotes the intensity of the deviatoric part of  $\varepsilon$ :

$$Q_\varepsilon = (2\bar{\Pi}_\varepsilon)^{1/2} \text{ with } \bar{\Pi}_\varepsilon = \frac{1}{2} \text{trace}(\varepsilon \cdot \varepsilon) - \frac{(\text{trace}(\varepsilon))^2}{6} \quad (23)$$

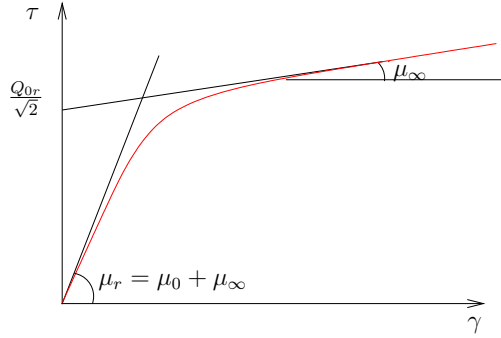


Figure 19: Material parameters involved in the hyperelastic law proposed by Favier et al. <69; 70> during a pure shear test.

724 To determine the influence of this behavioural law, numerical comparisons  
 725 were performed on the displacement of the cushion and its stress distribution  
 726 in the case of both this non linear evolution and an equivalent elastic law.  
 727 The stress-strain curves obtained with both of these two laws are presented  
 728 in fig. 20 and compared with those obtained a uniaxial tensile test performed  
 729 in <71> at a strain-rate of 3.6%/min on a film with the same thickness as  
 730 that of which this cushion was made.

731 The material parameters involved in these two laws are presented in ta-  
 732 ble 2. Contrary to the test on a cushion described in section 4.3, a pressure  
 733 of 2 kPa was applied here to a square cushion 2000 mm in length and 0.25  
 734 mm thick. Due to the symmetry, only an eighth of the square was simulated.

735 These simulations were performed with a mesh consisting of  $15 \times 15$  quadrangular elements, using linear interpolation methods. The value of parameter  
736  $\lambda$  involved in the DR method was set at 3.

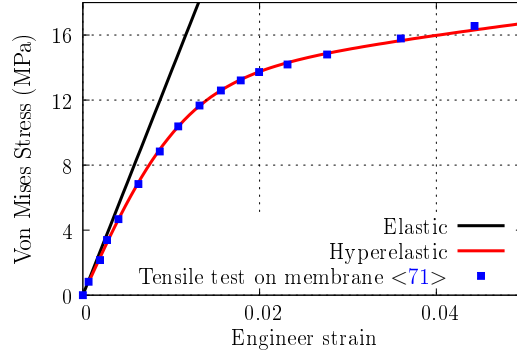


Figure 20: Comparison between the elastic and hyperelastic responses during a uniaxial tensile test presented in <71>.

737

Elastic parameters		Favier's Hyperelastic parameters			
E (MPa)	$\nu$	$K$ (MPa)	$Q_{or}$ (MPa)	$\mu_r$ (MPa)	$\mu_\infty$ (MPa)
1375	0.4	3000	10.5	430	35

Table 2: Material parameters of the elastic and hyperelastic laws used to simulate the inflation of a cushion.

738 The global equilibria obtained with the two laws can be compared in  
739 Figure 21a. This figure gives the vertical displacement of the symmetrical  
740 horizontal line of the cushion at the end of the inflation. The shape of the  
741 cushion is almost identical with both the elastic and hyperelastic laws. The  
742 evolution of the major principal stress  $\sigma_1$  along the symmetrical horizontal  
743 line of the cushion is presented in fig. 21b. The non-linearity of the hyper-  
744 elastic law results in a different pattern of stress distribution, especially in  
745 the centre of the cushion. However, it is worth noting that the location of

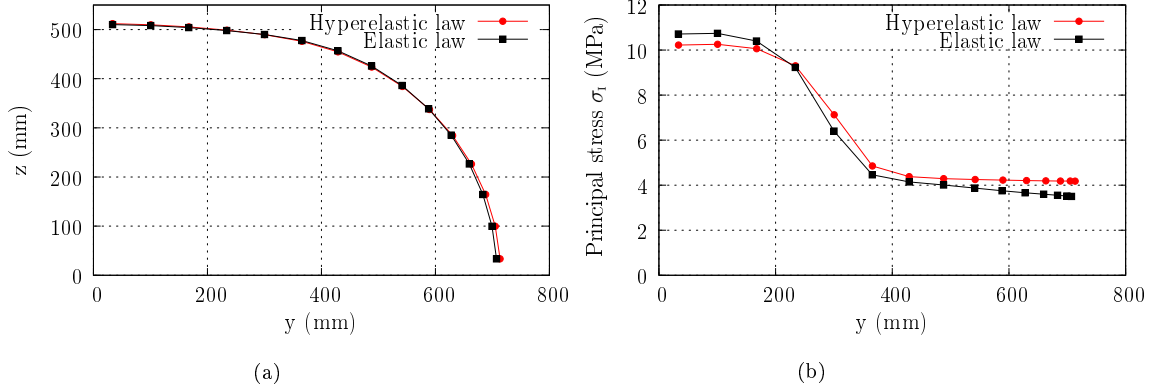


Figure 21: (a) Vertical displacement and (b) Evolution of the major principal stress  $\sigma_I$  along the symmetrical horizontal line of the cushion with elastic and hyperelastic laws.

the wrinkles is independent of the constitutive law used. Their location is similar to that previously observed in fig. 16a.

## 5. Application of the PS–DPS model: Zero Pressure Balloon inflation

In this section, the inflation of a Zero Pressure Balloon (ZPB) is simulated using the PS–DPS model both with an elastic law and with the same hyperelastic law as in the previous section.

During stratospheric missions, the volume of these balloons depends on their altitude (see fig. 22.a). These variations are caused by changes of temperature and pressure inside the balloons. At the start of the take-off and throughout these missions (see fig. 22.b), the wrinkles on the balloon continue to evolve. Accounting numerically for wrinkles in these structures is particularly important because the gas pressure, which depends on the volume of the balloon, affects the stress field. The DR method has often been used to simulate these inflation and wrinkle processes <40; 53–56>.

To test the validity the operation of the model and investigate the impact

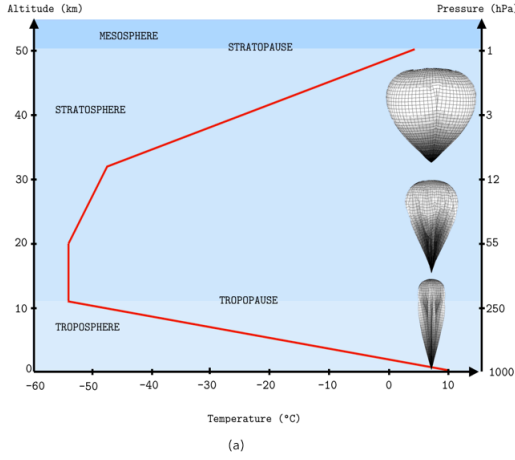


Figure 22: (a) Evolution of the pressure and temperature during a flight mission. (b) Photo of a ZPB before take-off [72](#).

of wrinkles on a real structure, equilibrium configurations were calculated during all the phases of a ZPB flight (during take-off and flight, depending on the altitude and the internal pressure) using both elastic and hyperelastic laws. The numerical conditions used in the simulations are presented in fig. [23](#) and table [3](#).

The ZPB is composed of 74 gores, but only one gore of the balloon was simulated, and conditions of cyclic symmetry were imposed on the edges of the gore in order to account for this hypothesis. The gores, which are made of an LLDPE film, are assembled with polyester fiber reinforced tapes. In the case of these large-sized balloons, the main load to be simulated is the pressure gradient  $\Delta p$  in the balloon, which reflects the effects of the gas on the film. This gradient is calculated by subtracting the pressure in the balloon from the external pressure. It depends on the balloon's altitude  $z$ , which is an input parameter in the simulation and the thickness  $h$  of the film. The weight of the film and that of the tapes is accounted for in the simulations by a loading gravity condition. The mass of the pole piece (9.2 kg) is significant

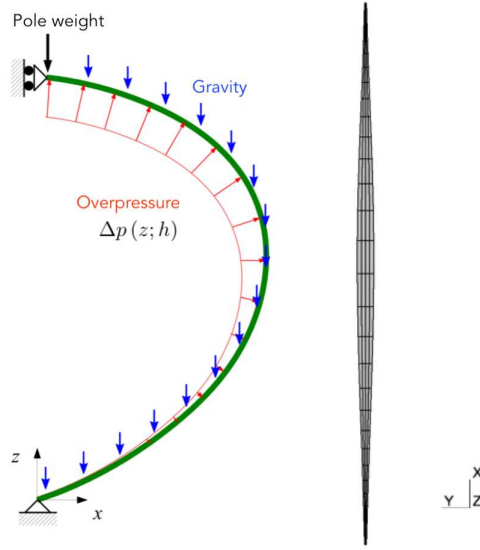


Figure 23: Mesh and loads applied during the ZPB simulations <73>.

Properties	Film	Tapes
Young's modulus (MPa)	1883	5986
Thickness $h$ ( $\mu\text{m}$ )	25	-
Poisson's ratio	0.45	0.3
Density $\rho$ ( $\text{kg}/\text{m}^3$ )	913	830

(a) Film's and tapes' elastic properties

Favier's hyperelastic parameters of the film			
$K$ (MPa)	$Q_{or}$ (MPa)	$\mu_r$ (MPa)	$\mu_\infty$ (MPa)
1000	18.95	614.17	0.6

(b) Hyperelastic parameters used to model the film

Table 3: Material properties of the film and tapes.

778 since it affects the shape of the balloon, and it is therefore simulated here in  
779 terms of its weight in the form of vertical point forces applied to the nodes  
780 at the end of the gore. These various loads and the mesh used are presented

781 in fig. 23. This mesh is composed of 120 quadrangular elements with linear  
782 interpolation, and 90 bar elements with linear interpolation stand for the  
783 assembly tapes. These tapes are located in the middle of the gore with an  
784 equivalent section of  $9.586 \text{ mm}^2$ . The contact between film and tapes is  
785 assumed to be perfect.

786 To simulate all the phases in the ZPB inflation process, two stages are  
787 defined:

- 788 1. The first stage consists in inflating the gore by applying the hydrostatic  
789 pressure gradually until the maximum altitude of 32.5 km is reached.  
790 During this phase, the boundary conditions for the hook and pole are  
791 applied but not the conditions of cyclic symmetry. The parameter  $\lambda$  in  
792 the DR method is set at 0.6. To speed up the calculation time, only  
793 the PS model is used at the start of the calculation. At the end of this  
794 step, the PS–DPS model is activated.
- 795 2. The second stage consists in applying the conditions of cyclic symme-  
796 try by means of linear boundary conditions. During this stage, the  
797 parameter  $\lambda$  is set at 2 and 12 with the elastic and hyperelastic law,  
798 respectively.

799 *Comment 1.* The initial configuration is the flat shape of the gore.

800 *Comment 2.* The parameter  $\lambda$  involved in the DR method is greatly increased  
801 in the case of the hyperelastic model because the non-linear part gives rise  
802 to many kinetic peaks at the end of the simulation.

803 Figure 24a shows the shape of the balloon with the PS and PS–DPS  
804 models in the case of elastic behaviour and with the PS–DPS model using  
805 the hyperelastic model. The overall shape of the gore differs slightly between  
806 the models tested because modelling a single gore of the balloon constrains



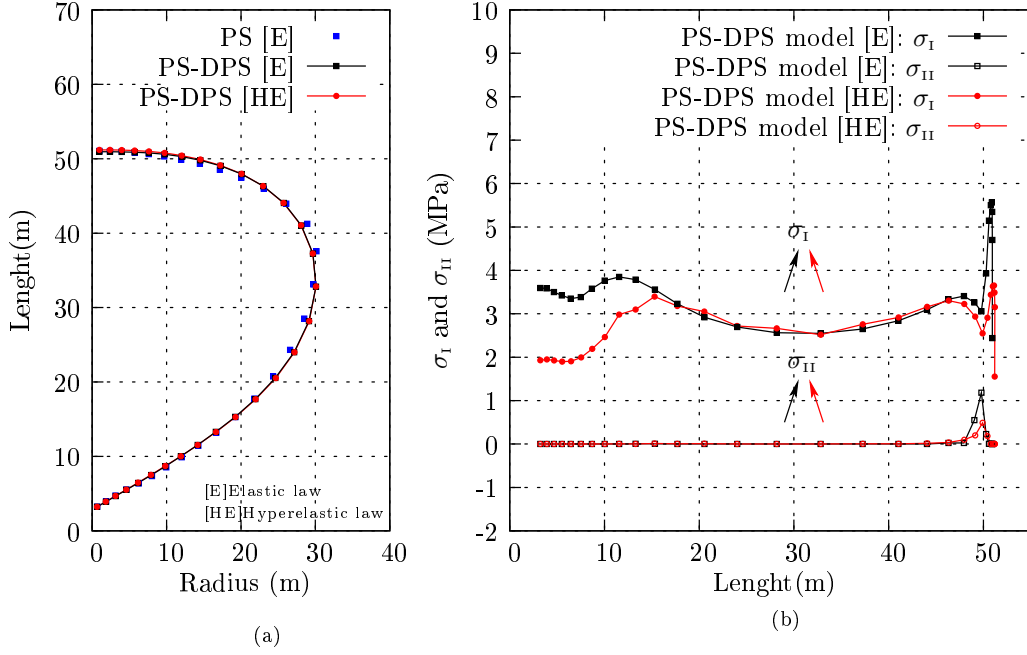


Figure 24: (a) Comparison on the ZPB shape between the PS and PS-DPS models, depending on the behavioural laws used. (b) Comparison on the local stress equilibrium in the ZPB between the elastic law [E] and the hyperelastic law [HE] with the PS-DPS model.

the shape of the final gore, which results in a slight difference in the overall shape depending on the type of law used. The major and minor principal stresses  $\sigma_{I_{max}}$  and  $\sigma_{II_{min}}$  in all the gores are presented in table 4. Contrary to the shape, the stress field differs considerably between the PS and PS-DPS models. During these simulations, the ZPB is not very heavily loaded mechanically. However, contrary to results obtained with the PS-DPS model, stress patterns obtained with the PS model are greatly disturbed by the presence of wrinkles on the balloon, which shows that taking these wrinkles into account greatly affects the simulations. The distribution of the major and minor principal stresses along the middle of the gore with the PS-DPS model are presented in fig. 24b. The stress levels obtained with the elastic

818 and hyperelastic laws are very low in these cases. However, the top and  
819 bottom of the balloon are the places where the films are the most heavily  
loaded, and where the influence of the constitutive law is the strongest.

	Elastic law		Hyperelastic law
	PS model	PS–DPS model	PS–DPS model
$\sigma_{IImin}$ (MPa)	-1820.	0.	0.
$\sigma_{IImax}$ (MPa)	115	5.56	3.65
Computation time for one iteration in the second stage (s/it)	0.150	0.542	1.097

Table 4: Major and minor principal stresses obtained in all the surface of the ZPB with the PS and PS–DPS models. Impact of the behavioural law used on the computational time in the case of a balloon.

820

821 The results of the stress fields presented in the table 4 and the figure 24b  
822 are in adequacy with the numerical results of the balloons of the same types  
823 <74; 75>. However, the materials, the number of balloon gores, the tapes  
824 assemblies used and the weight carried during a mission make comparisons  
825 between studies difficult.

826 Figure 25 shows the kinetic energy versus the iterations performed during  
827 the final stage in the calculations (pressure at the altitude targeted, activation  
828 of the wrinkling model in two cases). With the PS model, the evolution of  
829 the kinetic energy is very pronounced between each peak. Table 4 shows  
830 the time required by the two models to perform an iteration in this final  
831 stage. In the case of the PS model, this time was 0.15 s in the case of the  
832 elastic law, but 3.6 times longer in that of the PS–DPS model. However,  
833 contrary to the PS–DPS model, a larger number of iterations was necessary

834 to reach convergence with the PS model, but the time required was very short  
 835 due to the simplicity of the elastic law used. When the balloon is inflated  
 836 without using the wrinkling model, the local stress field is very noisy because  
 837 of the presence of these wrinkles. Balancing these internal stresses can be  
 838 detrimental to the convergence with the PS model, whereas the number of  
 839 iterations required to reach convergence is much smaller with the PS–DPS  
 model.

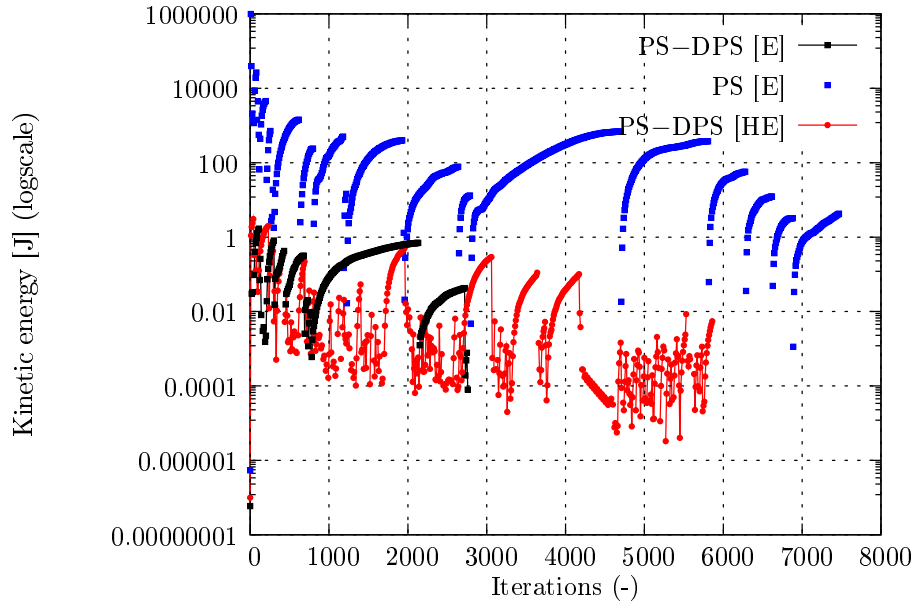


Figure 25: Evolution of the kinetic energy in the last step of the calculations in the case of the PS–DPS model with an elastic law and a hyperelastic law and that of the PS model with an elastic law.

840

841 The use of the non-linear hyperelastic law and the PS–DPS model yielded  
 842 many peaks in the kinetic energy. The evolution of the kinetic energy between  
 843 peaks was less visible than with the other models with a linear law. However,  
 844 despite the increase observed in the  $\lambda$  factor (which increased by 6 fold in  
 845 comparison with the elastic law), the simulation was still rather unstable.  
 846 The calculation time required for each iteration was twice as long as with

the PS–DPS model with an elastic law. During this simulation, the kinetic damping used in the DR algorithm was found to slow down the convergence. In fact, a large number of kinetic energy peaks was always observed, especially at the end of the calculation. This somewhat chaotic nature of the kinetic damping may be increased by the non-linear law used to simulate the film. These results therefore show that the long computational times are mainly due to the complexity of the non-linear law used in this case, which also gives rise to convergence problems

These simulations point to the conclusion that the use of the PS–DPS and PS models is indicated on real-life structures. They show that the local stresses at work in the structure are more intense and differently distributed when complex behavioural laws are used in the simulations. In the context of stratospheric balloons, the use of a non-linear model resembling real-life behaviour more closely is essential to the successful design and development of these structures. The possibility of using a wrinkling model with more complex constitutive laws provides the most reliable means of predicting balloons’ process of inflation during their missions.

## 6. Conclusion and outlook

A new wrinkling model named the PS-DPS model, which can be used with non-linear behaviour of all kinds is presented here. This model, based on the Almansi strain involves the use of a pseudo-Dynamic Relaxation method to determine the shape of flexible structures. Two plane stress conditions are imposed to simulate the wrinkled part in a state of uniaxial tension on the plane of the membrane. This model was first tested with a linear elastic behavioural law on numerical data in the literature in order to check its efficiency in classical cases. Lastly, the PS-DPS model was used to simulate the

inflation of a zero pressure balloon and found to be compatible with complex laws such as non-linear hyperelastic behavioural laws on real-life structures. A constitutive model of this kind was found to be the most suitable for describing the mechanical behaviour of the films of which stratospheric balloons are made.

Further studies on the PS-DPS model are also under way in order to improve its responses when used with incremental anisotropic laws. Another drawback observed when the pseudo-Dynamic Relaxation method was used with complex constitutive laws is that the time to convergence required to determine local equilibria is very long. In addition, with the wrinkling model, the computational time tends to be slightly longer than with a so-called conventional membrane model. It is therefore now proposed to develop new numerical strategy in future studies in order to reduce the computational time requirements of the model, especially when a complex behavioural law is used

#### **CRedit author statement**

**H. Le Meitour:** Validation, Investigation, Formal analysis, Writing - original draft. **G. Rio:** Conceptualization, Methodology, Investigation, Software, Writing - review & editing, Supervision. **H. Laurent:** Investigation, Writing - review & editing, Visualization, Resources, Funding acquisition, Supervision. **A. S. Lectez:** Data Curation, Resources, Writing - review & editing, Supervision. **P. Guigue:** Project administration, Funding acquisition, Supervision.

## 896 Acknowledgements

897 This research was supported by the CNES (team DSO/BL/VP),  
898 the company CNIM AIR SPACE and the Brittany Region  
899 (MITOFERM:0461/ARE11219/00030953) under contract N° 2840-  
900 2841/2017-00721. The authors would like to thank Julien Troufflard  
901 (a freelance engineer) and Frank Petitjean from the company [RTIME](#) for  
902 their useful suggestions and discussions.

## 903 Appendices

904 To clarify the following calculations of the tangent matrices, the following  
905 notations have been introduced: "3D" for the general 3D behaviour, "PS"  
906 for the specific 2D Plane Stress and "DPS" for the specific 1D Plane Stress  
907 when wrinkles occur.

### 908 A. Calculation of the tangent matrix in the PS model

909 When modelling the membrane, the plane stress condition has to be al-  
910 ways satisfied, that is:  $\sigma_{PS}^{33}(\varepsilon_{33}) = 0$ . The differential therefore also has to  
911 be zero:  $d\sigma_{PS}^{33}(\varepsilon_{33}) = 0$

Due to the method used to enforce the plane stress, the  $\varepsilon_{33(t+\Delta t)}$  obtained  
is in fact an implicit function of the in-plane deformations  $\varepsilon_{\gamma\eta}$  where  $\gamma, \eta =$   
1 and 2 and we can write:

$$0 = \frac{\partial \sigma^{33}}{\partial \varepsilon_{\gamma\eta}}(PS) = \frac{\partial \sigma^{33}}{\partial \varepsilon_{\gamma\eta}}(3D) + \frac{\partial \sigma^{33}}{\partial \varepsilon_{33}}(3D) \frac{\partial \varepsilon_{33}}{\partial \varepsilon_{\gamma\eta}}$$

which leads to the relations:

$$\frac{\partial \varepsilon_{33}}{\partial \varepsilon_{\gamma\eta}} = - \left[ \frac{\partial \sigma^{33}}{\partial \varepsilon_{33}}(3D) \right]^{-1} \frac{\partial \sigma^{33}}{\partial \varepsilon_{\gamma\eta}}(3D)$$

which are used to obtain the tangent matrix (where  $\alpha, \beta = 1$  and 2):

$$\frac{\partial \sigma^{\alpha\beta}}{\partial \varepsilon_{\gamma\eta}}(PS) = \frac{\partial \sigma^{\alpha\beta}}{\partial \varepsilon_{\gamma\eta}}(3D) + \frac{\partial \sigma^{\alpha\beta}}{\partial \varepsilon_{33}}(3D) \frac{\partial \varepsilon_{33}}{\partial \varepsilon_{\gamma\eta}}$$

## 912 B. Calculation of the tangent matrix in the PS-DPS model

913 The general expression for the tangent matrix is:

$$\frac{\partial \sigma^{ef}}{\partial \varepsilon_{kl}}(DPS) = \frac{\partial \sigma^{ef}}{\partial \varepsilon_{kl}}(3D) + \frac{\partial \sigma^{ef}}{\partial \varepsilon_{gh}}(3D) \frac{\partial \varepsilon_{gh}}{\partial \varepsilon_{kl}} \quad (24)$$

where  $e, f = 2$  and 3. The degrees of freedom of the DPS condition in the present case are  $\varepsilon_{ee}$ , where  $e = 2$  and 3. In this context, the relevant unknowns in relation (24) are the values of  $\frac{\partial \varepsilon_{ee}}{\partial \varepsilon_{11}}$ . We use the conditions  $\sigma^{ee} = 0$  that must always be satisfied in DPS to calculate these values :

$$\frac{\partial \sigma^{ee}}{\partial \varepsilon_{11}}(DPS) = 0 = \frac{\partial \sigma^{ee}}{\partial \varepsilon_{11}}(3D) + \frac{\partial \sigma^{ee}}{\partial \varepsilon_{ff}}(3D) \frac{\partial \varepsilon_{ff}}{\partial \varepsilon_{11}}$$

and hence:

$$\frac{\partial \varepsilon_{ff}}{\partial \varepsilon_{11}} = - \left[ \frac{\partial \sigma^{ee}}{\partial \varepsilon_{ff}}(3D) \right]^{-1} \frac{\partial \sigma^{ff}}{\partial \varepsilon_{11}}(3D)$$

The final tangent operator can then be calculated as follows:

$$\frac{\partial \sigma^{11}}{\partial \varepsilon_{11}}(DPS) = \frac{\partial \sigma^{11}}{\partial \varepsilon_{11}}(3D) + \frac{\partial \sigma^{11}}{\partial \varepsilon_{ff}}(3D) \frac{\partial \varepsilon_{ff}}{\partial \varepsilon_{11}}$$

914

915 **References**

- 916 [1] C. H. Jenkins, Nonlinear Dynamic Response of Membranes: State of  
917 the Art - Update, Appl. Mech. Rev 49 (10S) (1996) S41–S48. doi:  
918 [10.1115/1.3101975](https://doi.org/10.1115/1.3101975).
- 919 [2] A. Adler, M. Mikulas, Application of a wrinkled membrane finite element  
920 approach to advanced membrane structures, American Institute of Aero-  
921 nautics and Astronautics. (Aug. 2001). doi:[10.2514/6.2001-4646](https://doi.org/10.2514/6.2001-4646).
- 922 [3] W. Wong, S. Pellegrino, Wrinkled membranes III: numerical simulations,  
923 Journal of Mechanics of Materials and Structures 1 (1) (2006) 63–95.  
924 doi:[10.2140/jomms.2006.1.63](https://doi.org/10.2140/jomms.2006.1.63).
- 925 [4] A. Jarasjarungkiat, R. Wüchner, K. U. Bletzinger, A wrinkling model  
926 based on material modification for isotropic and orthotropic membranes,  
927 Computer Methods in Applied Mechanics and Engineering 197 (6)  
928 (2008) 773–788. doi:[10.1016/j.cma.2007.09.005](https://doi.org/10.1016/j.cma.2007.09.005).
- 929 [5] S. Kumar, S. H. Upadhyay, A. C. Mathur, Wrinkling Simulation of  
930 Membrane Structures under Tensile and Shear Loading, Journal of Vi-  
931 bration Analysis, Measurement, and Control 3 (1) (2015) 17. doi:  
932 [10.7726/jvamc.2015.1002](https://doi.org/10.7726/jvamc.2015.1002).
- 933 [6] X. F. Wang, Q. S. Yang, S.-s. Law, Wrinkled membrane element based  
934 on the wrinkling potential, International Journal of Solids and Struc-  
935 tures 51 (21) (2014) 3532–3548. doi:[10.1016/j.ijsolstr.2014.06.](https://doi.org/10.1016/j.ijsolstr.2014.06.004)  
936 [004](https://doi.org/10.1016/j.ijsolstr.2014.06.004).
- 937 [7] Y. Miyazaki, Wrinkle/slack model and finite element dynamics of mem-  
938 brane, International Journal for Numerical Methods in Engineering  
939 66 (7) (2006) 1179–1209. doi:[10.1002/nme.1588](https://doi.org/10.1002/nme.1588).



- 940 [8] X. Wang, S.-s. Law, Q. Yang, N. Yang, Numerical study on the dynamic  
941 properties of wrinkled membranes, *International Journal of Solids and*  
942 *Structures* 143 (2018) 125–143. doi:10.1016/j.ijsolstr.2018.03.  
943 001.
- 944 [9] X. Deng, Y. Xu, C. Clarke, Wrinkling modelling of space membranes  
945 subject to solar radiation pressure, *Composites Part B: Engineering*.  
946 (Aug. 2018). doi:10.1016/j.compositesb.2018.08.088.
- 947 [10] H. Wagner, Flat sheet metal girders with very thin metal web. Part I :  
948 : general theories and assumptions, National Advisory Committee for  
949 Aeronautics, 1931, oCLC: 919168471.  
950 URL [http://app.knovel.com/hotlink/toc/id:kpFSMGVT11/](http://app.knovel.com/hotlink/toc/id:kpFSMGVT11/flat-sheet-metal)  
951 [flat-sheet-metal](http://app.knovel.com/hotlink/toc/id:kpFSMGVT11/flat-sheet-metal)
- 952 [11] E.-S. Lee, S.-K. Youn, Finite element analysis of wrinkling membrane  
953 structures with large deformations, *Finite Elements in Analysis and De-*  
954 *sign* 42 (8-9) (2006) 780–791. doi:10.1016/j.finel.2006.01.004.
- 955 [12] D. G. Roddeman, Finite-element analysis of wrinkling membranes,  
956 *Communications in Applied Numerical Methods* 7 (4) (1991) 299–307.  
957 doi:10.1002/cnm.1630070408.
- 958 [13] C. H. Wu, T. R. Canfield, Wrinkling in finite plane-stress theory, *Quar-*  
959 *terly of Applied Mathematics* 39 (2) (1981) 179–199. doi:10.1090/qam/  
960 625468.
- 961 [14] A. C. Pipkin, The Relaxed Energy Density for Isotropic Elastic Mem-  
962 branes, *IMA Journal of Applied Mathematics* 36 (1) (1986) 85–99.  
963 doi:10.1093/imamat/36.1.85.

- 964 [15] E. M. Haseganu, D. J. Steigmann, Analysis of partly wrinkled mem-  
 965 branes by the method of dynamic relaxation, *Computational Mechanics*  
 966 14 (6) (1994) 596–614. [doi:10.1007/BF00350839](https://doi.org/10.1007/BF00350839).
- 967 [16] D. J. Steigmann, A. C. Pipkin, Finite deformations of wrinkled mem-  
 968 branes, *The Quarterly Journal of Mechanics and Applied Mathematics*  
 969 42 (3) (1989) 427–440. [doi:10.1093/qjmam/42.3.427](https://doi.org/10.1093/qjmam/42.3.427).
- 970 [17] T. Raible, K. Tegeler, S. Löhnert, P. Wriggers, Development of a wrin-  
 971 kling algorithm for orthotropic membrane materials, *Computer Meth-*  
 972 *ods in Applied Mechanics and Engineering* 194 (21) (2005) 2550–2568.  
 973 [doi:10.1016/j.cma.2004.07.045](https://doi.org/10.1016/j.cma.2004.07.045).
- 974 [18] M. Epstein, M. A. Forcinito, Anisotropic membrane wrinkling: the-  
 975 ory and analysis, *International Journal of Solids and Structures* 38 (30)  
 976 (2001) 5253–5272. [doi:10.1016/S0020-7683\(00\)00346-2](https://doi.org/10.1016/S0020-7683(00)00346-2).
- 977 [19] A. Jarasjarungkiat, R. Wüchner, K.-U. Bletzinger, Efficient sub-grid  
 978 scale modeling of membrane wrinkling by a projection method, *Com-*  
 979 *puter Methods in Applied Mechanics and Engineering* 198 (9-12) (2009)  
 980 1097–1116. [doi:10.1016/j.cma.2008.11.014](https://doi.org/10.1016/j.cma.2008.11.014).
- 981 [20] S. Kang, S. Im, Finite Element Analysis of Wrinkling Membranes, *Jour-*  
 982 *nal of Applied Mechanics* 64 (2) (1997) 263. [doi:10.1115/1.2787302](https://doi.org/10.1115/1.2787302).
- 983 [21] X. Liu, C. H. Jenkins, W. W. Schur, Large deflection analysis of pneu-  
 984 matic envelopes using a penalty parameter modified material model,  
 985 *Finite Elements in Analysis and Design* 37 (3) (2001) 233–251. [doi:](https://doi.org/10.1016/S0168-874X(00)00040-8)  
 986 [10.1016/S0168-874X\(00\)00040-8](https://doi.org/10.1016/S0168-874X(00)00040-8).
- 987 [22] K. Woo, H. Igawa, C. H. Jenkins, Analysis of Wrinkling Behavior of

- 988 Anisotropic Membrane, CMES: Computer Modeling in Engineering &  
989 Sciences 6 (4) (2004) 397–408. [doi:10.3970/cmes.2004.006.397](https://doi.org/10.3970/cmes.2004.006.397).
- 990 [23] R. K. Miller, J. M. Hedgepeth, An algorithm for finite element analysis  
991 of partly wrinkled membranes, AIAA Journal 20 (12) (1982) 1761–1763.  
992 [doi:10.2514/3.8018](https://doi.org/10.2514/3.8018).
- 993 [24] R. K. Miller, J. M. Hedgepeth, V. I. Weingarten, P. Das, S. Kahyai, Fi-  
994 nite element analysis of partly wrinkled membranes, Computers & Struc-  
995 tures 20 (1) (1985) 631–639. [doi:10.1016/0045-7949\(85\)90111-7](https://doi.org/10.1016/0045-7949(85)90111-7).
- 996 [25] A. Adler, M. Mikulas, J. Hedgepeth, Static and dynamic analysis of  
997 partially wrinkled membrane structures, in: 41st Structures, Structural  
998 Dynamics, and Materials Conference and Exhibit, American Institute of  
999 Aeronautics and Astronautics, Atlanta, GA, U.S.A., 2000. [doi:10.2514/  
1000 6.2000-1810](https://doi.org/10.2514/6.2000-1810).
- 1001 [26] H. Ding, B. Yang, The modeling and numerical analysis of wrinkled  
1002 membranes, International Journal for Numerical Methods in Engineer-  
1003 ing 58 (12) (2003) 1785–1801. [doi:10.1002/nme.832](https://doi.org/10.1002/nme.832).
- 1004 [27] T. Akita, K. Nakashino, M. C. Natori, K. C. Park, A simple com-  
1005 puter implementation of membrane wrinkle behaviour via a projection  
1006 technique, International Journal for Numerical Methods in Engineering  
1007 71 (10) (2007) 1231–1259. [doi:10.1002/nme.1990](https://doi.org/10.1002/nme.1990).
- 1008 [28] L. Zheng, [Wrinkling of dielectric elastomer membranes](https://resolver.caltech.edu/CaltechETD:etd-09222008-161217), Ph.D. thesis,  
1009 California Institute of Technology, Pasadena, CA. (2009).  
1010 URL [http://resolver.caltech.edu/CaltechETD:  
1011 etd-09222008-161217](http://resolver.caltech.edu/CaltechETD:etd-09222008-161217)

- [29] E. Oñate, F. Zárte, Rotation-free triangular plate and shell elements, International Journal for Numerical Methods in Engineering 47 (1-3) (2000) 557–603. doi:[10.1002/\(SICI\)1097-0207\(20000110/30\)47:1/3<557::AID-NME784>3.0.CO;2-9](https://doi.org/10.1002/(SICI)1097-0207(20000110/30)47:1/3<557::AID-NME784>3.0.CO;2-9).
- [30] H. Laurent, G. Rio, Formulation of a thin shell finite element with continuity  $C^0$  and convected material frame notion, Computational Mechanics 27 (3) (2001) 218–232. doi:[10.1007/s004660100243](https://doi.org/10.1007/s004660100243).
- [31] F. G. Flores, E. Oñate, Improvements in the membrane behaviour of the three node rotation-free BST shell triangle using an assumed strain approach, Computer Methods in Applied Mechanics and Engineering 194 (6) (2005) 907–932. doi:[10.1016/j.cma.2003.08.012](https://doi.org/10.1016/j.cma.2003.08.012).
- [32] Y. Lecieux, R. Bouzidi, Experimental analysis on membrane wrinkling under biaxial load - Comparison with bifurcation analysis, International Journal of Solids and Structures 47 (18) (2010) 2459–2475. doi:[10.1016/j.ijsolstr.2010.05.005](https://doi.org/10.1016/j.ijsolstr.2010.05.005).
- [33] F. G. Flores, E. Oñate, Wrinkling and folding analysis of elastic membranes using an enhanced rotation-free thin shell triangular element, Finite Elements in Analysis and Design 47 (9) (2011) 982–990. doi:[10.1016/j.finel.2011.03.014](https://doi.org/10.1016/j.finel.2011.03.014).
- [34] T. Iwasa, Approximate estimation of wrinkle wavelength and maximum amplitude using a tension-field solution, International Journal of Solids and Structures 121 (2017) 201 – 211. doi:[10.1016/j.ijsolstr.2017.05.029](https://doi.org/10.1016/j.ijsolstr.2017.05.029).
- [35] P. Contri, B. A. Schrefler, A geometrically nonlinear finite element analysis of wrinkled membrane surfaces by a no-compression material

- 1037 model, *Communications in Applied Numerical Methods* 4 (1) (1988)  
1038 5–15. [doi:10.1002/cnm.1630040103](https://doi.org/10.1002/cnm.1630040103).
- 1039 [36] T. Gerngross, S. Pellegrino, Anisotropic Viscoelasticity and Wrinkling of  
1040 Superpressure Balloons: Simulation and Experimental Verification, in:  
1041 AIAA Balloon Systems Conference, BLN-6: Materials and Structures  
1042 II, 2009. [doi:10.2514/6.2009-2815](https://doi.org/10.2514/6.2009-2815).
- 1043 [37] T. Gerngross, Y. Xu, S. Pellegrino, Viscoelastic behaviour of pumpkin  
1044 balloons, *Advances in Space Research* 42 (10) (2008) 1683–1690. [doi:](https://doi.org/10.1016/j.asr.2007.03.093)  
1045 [10.1016/j.asr.2007.03.093](https://doi.org/10.1016/j.asr.2007.03.093).
- 1046 [38] X. Deng, S. Pellegrino, Wrinkling of orthotropic viscoelastic membranes,  
1047 *AIAA Journal* 50 (3) (2012) 668–681. [doi:10.2514/1.J051255](https://doi.org/10.2514/1.J051255).
- 1048 [39] K. Kwok, S. Pellegrino, Large strain viscoelastic model for balloon film,  
1049 in: AIAA (Ed.), 11th AIAA Aviation Technology, Integration, and Op-  
1050 erations (ATIO) Conference, American Institute of Aeronautics and As-  
1051 tronautics, 2011. [doi:10.2514/6.2011-6939](https://doi.org/10.2514/6.2011-6939).
- 1052 [40] D. Wakefield, A. Bown, Non-Linear Analysis of the NASA Super Pres-  
1053 sure Balloons: Some Detailed Investigations of Recent Antarctic Flight  
1054 Balloons, in: 11th AIAA Aviation Technology, Integration, and Opera-  
1055 tions (ATIO) Conference, American Institute of Aeronautics and Astro-  
1056 nautics, 2011. [doi:10.2514/6.2011-6829](https://doi.org/10.2514/6.2011-6829).
- 1057 [41] V. Nayyar, K. Ravi-Chandar, R. Huang, Stretch-induced stress patterns  
1058 and wrinkles in hyperelastic thin sheets, *International Journal of Solids*  
1059 *and Structures* 48 (25) (2011) 3471–3483. [doi:10.1016/j.ijsolstr.](https://doi.org/10.1016/j.ijsolstr.2011.09.004)  
1060 [2011.09.004](https://doi.org/10.1016/j.ijsolstr.2011.09.004).

- 1061 [42] C. Fu, T. Wang, F. Xu, Y. Huo, M. Potier-Ferry, A modeling and reso-  
 1062 lution framework for wrinkling in hyperelastic sheets at finite membrane  
 1063 strain, *Journal of the Mechanics and Physics of Solids* 124 (2019) 446–  
 1064 470. [doi:10.1016/j.jmps.2018.11.005](https://doi.org/10.1016/j.jmps.2018.11.005).
- 1065 [43] R. Ziegler, W. Wagner, K.-U. Bletzinger, A Finite Element Model  
 1066 for the Analysis of Wrinkled Membrane Structures, *International*  
 1067 *Journal of Space Structures* 18 (1) (2003) 1–14. [doi:10.1260/](https://doi.org/10.1260/026635103769016591)  
 1068 [026635103769016591](https://doi.org/10.1260/026635103769016591).
- 1069 [44] M. R. Barnes, Form Finding and Analysis of Tension Structures by  
 1070 Dynamic Relaxation, *International Journal of Space Structures* 14 (2)  
 1071 (1999) 89–104. [doi:10.1260/0266351991494722](https://doi.org/10.1260/0266351991494722).
- 1072 [45] P. Underwood, Dynamic Relaxation, in *Computational methods for*  
 1073 *transient analysis*. Eds T. Belytschko, T. J.R. Hugues. Elsevier Sci-  
 1074 *ence Publishers Amsterdam : North-Holland.*, 1983, Ch. 5, pp. 245–265.  
 1075 [doi:10.1002/zamm.19860660905](https://doi.org/10.1002/zamm.19860660905).
- 1076 [46] G. Rio (Ed.), Herezh++: FEM software for large transformations in  
 1077 solids, Université de Bretagne Sud, dépôt APP (Agence pour la Protec-  
 1078 tion des Programmes) - Certification IDDN-FR-010-0106078-000-R-P-  
 1079 2006-035-20600, 2006.
- 1080 [47] H. Laurent, G. Rio, A. Vandenbroucke, N. Aït Hocine, Experimental  
 1081 and numerical study on the temperature-dependent behavior of a fluoro-  
 1082 elastomer, *Mechanics of Time-Dependent Materials* 18 (4) (2014) 721–  
 1083 742. [doi:10.1007/s11043-014-9247-3](https://doi.org/10.1007/s11043-014-9247-3).
- 1084 [48] J. Troufflard, H. Laurent, G. Rio, B. Omnès, S. Javanaud, Temperature-  
 1085 dependent modelling of a HNBR O-ring seal above and below the glass

- 1086 transition temperature, *Materials & Design* 156 (2018) 1–15. doi:10.  
1087 1016/j.matdes.2018.06.016.
- 1088 [49] Abaqus, ABAQUS/Standard User’s Manual, Version 6.14 (2014).
- 1089 [50] P. Y. Manach, G. Rio, Analysis of orthotropic behavior in convected  
1090 coordinate frames, *Computational Mechanics* 23 (5) (1999) 510–518.  
1091 doi:10.1007/s004660050430.
- 1092 [51] D. G. Roddeman, J. Drukker, C. W. J. Oomens, J. D. Janssen, The  
1093 Wrinkling of Thin Membranes: Part I—Theory, *J. Appl. Mech* 54 (4)  
1094 (1987) 884–887. doi:10.1115/1.3173133.
- 1095 [52] J. Troufflard, *Étude numérique et expérimentale des structures gon-*  
1096 *flables : applications aux gilets de sauvetage gonflables*, Phd thesis,  
1097 Lorient (Jan. 2011).  
1098 URL <http://www.theses.fr/2011LORIS223>
- 1099 [53] D. Wakefield, Numerical Modelling of Pumpkin Balloon Instability, in:  
1100 AIAA 5th ATIO and 16th Lighter-Than-Air Sys Tech. and Balloon Sys-  
1101 tems Conferences, American Institute of Aeronautics and Astronautics,  
1102 2005. doi:10.2514/6.2005-7445.
- 1103 [54] D. Wakefield, Numerical Investigations of Pumpkin Balloon Deployment  
1104 Stability, in: AIAA Balloon Systems Conference, American Institute of  
1105 Aeronautics and Astronautics, 2007. doi:10.2514/6.2007-2604.
- 1106 [55] D. Wakefield, Non-Linear Viscoelastic Analysis and the Design of Super  
1107 Pressure Balloons: Stress, Strain and Stability, in: AIAA Balloon Sys-  
1108 tems Conference, American Institute of Aeronautics and Astronautics,  
1109 2009. doi:10.2514/6.2009-2813.

- 1110 [56] D. Wakefield, A. Bown, Non-Linear Analysis of the NASA Super Pres-  
 1111 sure Balloons: Whole Flight Simulations, in: AIAA Balloon Systems  
 1112 Conference, American Institute of Aeronautics and Astronautics, 2017.  
 1113 [doi:10.2514/6.2017-3606](https://doi.org/10.2514/6.2017-3606).
- 1114 [57] J. R. Garcia, [Numerical study of dynamic relaxation methods and con-](#)  
 1115 [tribution to the modelling of inflatable lifejackets](#), Phd thesis, Université  
 1116 de Bretagne Sud (Dec. 2011).  
 1117 URL <https://tel.archives-ouvertes.fr/tel-00659669/document>
- 1118 [58] J. Rodriguez, G. Rio, J. M. Cadou, J. Troufflard, Numerical study of  
 1119 dynamic relaxation with kinetic damping applied to inflatable fabric  
 1120 structures with extensions for 3d solid element and non-linear behavior,  
 1121 Thin-Walled Structures 49 (11) (2011) 1468–1474. [doi:10.1016/j.tws.](https://doi.org/10.1016/j.tws.2011.07.011)  
 1122 [2011.07.011](https://doi.org/10.1016/j.tws.2011.07.011).
- 1123 [59] R. Courant, K. Friedrichs, H. Lewy, On the Partial Difference Equations  
 1124 of Mathematical Physics, IBM Journal of Research and Development  
 1125 11 (2) (1967) 215–234. [doi:10.1147/rd.112.0215](https://doi.org/10.1147/rd.112.0215).
- 1126 [60] Mansfield Eric Harold, Pugsley Alfred Grenville, Load transfer via a  
 1127 wrinkled membrane, Proceedings of the Royal Society of London. A.  
 1128 Mathematical and Physical Sciences 316 (1525) (1970) 269–289. [doi:](https://doi.org/10.1098/rspa.1970.0079)  
 1129 [10.1098/rspa.1970.0079](https://doi.org/10.1098/rspa.1970.0079).
- 1130 [61] J. Leifer, W. Belvin, Prediction of Wrinkle Amplitudes in Thin  
 1131 Film Membranes Using Finite Element Modeling, in: 44th  
 1132 AIAA/ASME/ASCE/AHS/ASC Structures, Structural Dynamics, and  
 1133 Materials Conference, Structures, Structural Dynamics, and Materials



- 1134 and Co-located Conferences, American Institute of Aeronautics and As-  
1135 tronautics, 2003. [doi:10.2514/6.2003-1983](https://doi.org/10.2514/6.2003-1983).
- 1136 [62] W. Wong, S. Pellegrino, Wrinkled membranes I: experiments, Journal  
1137 of Mechanics of Materials and Structures 1 (1) (2006) 3–25. [doi:10.](https://doi.org/10.2140/jomms.2006.1.3)  
1138 [2140/jomms.2006.1.3](https://doi.org/10.2140/jomms.2006.1.3).
- 1139 [63] W. Wong, S. Pellegrino, Wrinkled membranes II: analytical models.,  
1140 Journal of Mechanics of Materials and Structures 1 (1) (2006) 27–61.  
1141 [doi:10.2140/jomms.2006.1.27](https://doi.org/10.2140/jomms.2006.1.27).
- 1142 [64] M. M. Mikulas, [Behavior of a flat stretched membrane wrinkled by the](#)  
1143 [rotation of an attached hub](#), no. 30 p. in NASA TN D-2456, National  
1144 Aeronautics and Space Administration. Langley Research Center, Wash-  
1145 ington, D.C., 1964.  
1146 URL [//catalog.hathitrust.org/Record/011433642](https://catalog.hathitrust.org/Record/011433642)
- 1147 [65] K. Lu, M. Accorsi, J. Leonard, Finite element analysis of membrane  
1148 wrinkling, International Journal for Numerical Methods in Engineer-  
1149 ing 50 (5) (2001) 1017–1038. [doi:10.1002/1097-0207\(20010220\)50:](https://doi.org/10.1002/1097-0207(20010220)50:5<1017::AID-NME47>3.0.CO;2-2)  
1150 [5<1017::AID-NME47>3.0.CO;2-2](https://doi.org/10.1002/1097-0207(20010220)50:5<1017::AID-NME47>3.0.CO;2-2).
- 1151 [66] E. Reissner, [On Tension Field Theory](#), in: Fifth International Congress  
1152 on Applied Mechanics, 1938, pp. 88–92.  
1153 URL <https://books.google.fr/books?id=LUrNXwAACAAJ>
- 1154 [67] M. Stein, J. M. Hedgepeth, [Analysis of partly wrinkled membranes](#),  
1155 Washington, D.C. : National Aeronautics and Space Administration :  
1156 [For sale by the Office of Technical Services, Dept. of Commerce], 1961.  
1157 URL <https://trove.nla.gov.au/version/179471700>

- 1158 [68] X. Wang, J. Ma, S.-s. Law, Q. Yang, Numerical analysis of wrinkle-  
1159 influencing factors of thin membranes, *International Journal of Solids*  
1160 *and Structures* 97-98 (2016) 458–474. doi:10.1016/j.ijsolstr.2016.  
1161 07.004.
- 1162 [69] D. Favier, P. Guélin, P. Pegon, Thermomechanics of Hysteresis Effects  
1163 in Shape Memory Alloys, *MSF* 56-58 (1991) 559–564. doi:10.4028/  
1164 www.scientific.net/MSF.56-58.559.
- 1165 [70] M. Zrida, H. Laurent, G. Rio, S. Pimbert, V. Grolleau, N. Masmoudi,  
1166 C. Bradai, Experimental and numerical study of polypropylene behavior  
1167 using an hyper-visco-hysteresis constitutive law, *Computational Materi-*  
1168 *als Science* 45 (2) (2009) 516 – 527. doi:10.1016/j.commatsci.2008.  
1169 11.017.
- 1170 [71] C. Galliot, R. H. Luchsinger, Uniaxial and biaxial mechanical properties  
1171 of ETFE foils, *Polymer Testing* 30 (4) (2011) 356–365. doi:10.1016/  
1172 j.polymertesting.2011.02.004.
- 1173 [72] CNES, last accessed May 2020. [link].  
1174 URL <https://phototheque.cnes.fr>
- 1175 [73] F. Petitjean, G. Rio, A. Hamdani, X. Soors, *Simulation du comporte-*  
1176 *ment de ballons stratosphériques ouverts*, in: *CSMA 2015 - 12ème*  
1177 *Colloque National en Calcul des Structures*, Giens, France, 2015.  
1178 URL [https://hal.archives-ouvertes.fr/hal-01502302/file/](https://hal.archives-ouvertes.fr/hal-01502302/file/csma2015_FP_GR.pdf)  
1179 [csma2015\\_FP\\_GR.pdf](https://hal.archives-ouvertes.fr/hal-01502302/file/csma2015_FP_GR.pdf)
- 1180 [74] W. W. Schur, J. M. Simpson, *Finite element solution for the structural*  
1181 *behavior of a scientific balloon*, *Advances in Space Research* 13 (2)  
1182 (1993) 45–48. doi:10.1016/0273-1177(93)90273-E.

1183 URL [http://www.sciencedirect.com/science/article/pii/](http://www.sciencedirect.com/science/article/pii/027311779390273E)  
1184 [027311779390273E](http://www.sciencedirect.com/science/article/pii/027311779390273E)

1185 [75] W. W. Schur, [Structural response of a zero-pressure balloon with an](#)  
1186 [axial load tendon](#), in: International Balloon Technology Conference,  
1187 Balloon Systems Conferences, American Institute of Aeronautics and  
1188 Astronautics, 1997. doi:10.2514/6.1997-1475.  
1189 URL <https://arc.aiaa.org/doi/10.2514/6.1997-1475>